signature supervisor

TECHNISCHE
UNIVERSITÄT
WIEN
Vienna University of Technology

DIPLOMA THESIS

Assessing activity-specific fracture risk in femora with metastatic lesions

executed to obtain the academic degree
Master of Science (MSc./Dipl.Ing.) under the supervision of

Univ.Prof. Dipl.-Ing. Dr.techn. Dieter H. Pahr &
Dipl.-Ing. Dr.techn. Alexander Synek

at the
Institute of Lightweight Design and Structural Biomechanics
Gumpendorfer Straße 7, BE

submitted to TU Wien
Faculty of Mechanical and Industrial Engineering

by

Luisa Victoria Scheuring, BSc.

May 22, 2025

signature student

Acknowledgements

First and foremost, I would like to express my deepest gratitude to my advisor, Alex, for his invaluable guidance, support and creative ideas throughout this thesis. His expertise has been instrumental in shaping this thesis and encouraged me to aim high — especially when it comes to presentations.

A big thank you also to Prof. Dieter Pahr for his input and for asking the kind of questions that made me realize I needed better answers. I appreciate your time and sharp eye.

Also, a big thank you to Prof. Elgeti for the support, guidance and ice cream supply on a Friday at the institute.

To my labmates at the FE-Lab, Carina and Günther, thank you for sitting with me in this wonderful room at 30 to 40 degrees and sharing cake with me, whenever it was most needed.

To my wonderful friends – thank you for always reminding me there's a life outside of uni and work, that i love to spend with you guys.

Most importantly,to my mum, dad, Maxi, Laurenz and Lukas: Your unconditional love, support and belief in me carried me through the toughest moments. Without you, this would not have been possible and I'm so grateful to have you by my side.

And finally, to coffee, deadlines and sheer panic: without you, this thesis would not exist.

Declaration in Lieu of Oath

I declare in lieu of oath, that I wrote this thesis and performed the associated research myself, using only literature cited in this volume. If text passages from sources are used literally, they are marked as such.

I confirm that this work is original and has not been submitted elsewhere for any examination, nor is it currently under consideration for a thesis elsewhere.

During the preparation of this work the author used ChatGPT (GPT4-turbo) for language editing. After using this tool/service, the author reviewed and edited the content as needed and take full responsibility for the content of the published article.

I acknowledge that the submitted work will be checked electronically-technically using suitable and state-of-the-art means (plagiarism detection software). On the one hand, this ensures that the submitted work was prepared according to the high-quality standards within the applicable rules to ensure good scientific practice 'Code of Conduct' at the TU Wien. On the other hand, a comparison with other student theses avoids violations of my personal copyright.

Luisa Scheuring, BSc.

Vienna, May 22, 2025

Abstract

Background: Metastatic bone disease involving the femur can lead to spontaneous fractures during daily activities. Activity-specific fracture risk prediction, for example during gait, could help to preserve patients' quality of life. While Finite Element (FE) models have been used under simplified conditions to assess fracture risk in intact femora, their accuracy for femora with metastatic lesions remains uncertain. Therefore, this study compares the fracture risk predictions of a simplified FE model, only including the peak hip joint load, with that of a physiological FE model, considering muscle- and hip joint forces of the whole gait cycle.

Methodology: The simulations were conducted based on an intact femur Computed Tomography (CT) scan of a female (58 years). 93 variations of this CT scan were created by randomly inserting lytic lesions. For the physiological FE model, muscle- and hip joint forces were computed for a full gait cycle using a musculoskeletal model (OpenSim, Gait 2392). All 93 CT scans were converted into voxel-based nonlinear FE models with an elasto-plastic material, applying boundary conditions following literature. For the simplified FE models, the femora were shortened to approximately 30 % of their original length and only the peak hip joint load of the musculoskeletal simulation was applied. In both FE model approaches, bones were classified as "fractured" in case of a plastic displacement of the hip joint centre of at least 0.1 mm.

Results: The fracture risk predictions of the two model types agreed in 90.32 % of cases. Prediction disagreement was predominantly associated with lesions located in the proximal femoral shaft or in the intertrochanteric region.

Conclusion: Given the high level of agreement in fracture risk prediction between the simplified and physiological FE model during gait, it can be concluded that the simplified model offers a promising prognostic tool that combines predictive accuracy with clinical applicability. However, the study needs to be extended to verify these results for multiple subjects and different activities of daily living.

Kurzfassung

Hintergrund: Metastatische Knochentumoren im Femur können bereits bei alltäglichen Aktivitäten zu spontanen Frakturen führen. Eine aktivitätsbezogene Frakturrisikovorhersage, etwa für das Gehen, könnte dazu beitragen, die Lebensqualität betroffener Patienten zu erhalten. Bisher verwendet man bei gesunden Femora häufig Finite-Elemente (FE)-Modelle unter Zugrundelegung vereinfachter Bedingungen zur Frakturrisikovorhersage; deren Genauigkeit ist bei Femora mit metastatischen Läsionen allerdings ungewiss. Daher vergleicht diese Studie die Frakturrisikovorhersage eines vereinfachten FE-Modells, das lediglich die maximale Hüftgelenkskraft berücksichtigt, mit der eines physiologischen FE-Modells, welches Muskel- und Hüftgelenkskräfte des ganzen Gangzykluses einbezieht.

Methodik: Die Grundlage der durchgeführten Simulationen bildete ein Computertomographie (CT)-Scan des gesunden Femurs einer 58-jährigen Frau. Durch Einfügen von zufällig platzierten und dimensionierten lytischen Läsionen wurden 93 Variationen dieses CT-Scans erstellt. Die Muskel- und Hüftgelenksbelastungen des Gangzykluses für das physiologische FE-Modell wurden mithilfe eines muskuloskelettalen Modells (OpenSim, Gait 2392) berechnet. Alle 93 CT-Scans wurden in voxelbasierte nichtlineare FE-Modelle mit elasto-plastischem Material umgewandelt, wobei Randbedingungen in Anlehnung an bestehende Literatur angewendet wurden. Für die vereinfachten FE-Modelle wurden die Femora auf ungefähr 30 % ihrer Länge gekürzt und nur die maximale Hüftgelenkslast der muskuloskelettalen Simulation angewendet. Bei beiden FE-Modellen galten Femora im Falle einer plastischen Verschiebung des Hüftgelenkszentrums von mindestens 0,1 mm als „frakturiert“.

Ergebnisse: Die Frakturrisikovorhersagen der beiden Modelltypen stimmten in 90,32 % der Fälle überein. Abweichungen traten vor allem bei Läsionen im proximalen Femurschaft oder im intertrochantären Bereich auf.

Conclusio: Aufgrund der hohen Übereinstimmung der Frakturrisikovorhersagen des vereinfachten und des physiologischen FE-Modells beim Gehen, lässt sich folgern, dass das vereinfachte Modell ein vielversprechendes Prognosemittel darstellt, welches Genauigkeit und klinische Anwendbarkeit vereint. Eine Ausweitung der Studie auf mehrere Personen und verschiedene Aktivitäten ist jedoch erforderlich, um die erhaltenen Ergebnisse zu verifizieren.

List of Figures

Contents

1 Introduction

1.1 Motivation

The skeleton is the third most commonly affected site by metastasis in the human body, predominantly originating from primary tumours in breast, prostate and lung [20, 88]. The femur is a frequent location for such metastatic lesions. Due to its weight-bearing function, the bone, specifically the proximal part, is prone to pathological fractures resulting from structural impairment caused by such lesions [20]. The fractures concerned are often caused by lytic lesions, which stimulate osteoclastic activity and inhibit osteoblastic bone formation [69].

As the pathology in question can lead to spontaneous fractures, the preventive measures impose considerable restrictions on the daily life of patients. Current clinical strategies, such as prophylactic fixation or general recommendations to reduce mobility, aim to minimize fracture risk [47, 22]. However, current clinical fracture risk assessment tools, like the Mirels' score [65], are limited in specificity and do not account for specific activities. Actual advice on currently feasible activities at the moment of medical examination could preserve independence and quality of life.

This independence also lies in daily activities such as walking, stair climbing, and standing up from a chair or bed. Moreover, physical exercise in general is important for muscle and bone structure and should be maintained if possible. *Guinan et al.* [46] reported that engaging in moderate-to-vigorous intense physical activities was associated with reduced pain and improved physical function for patients with metastatic bone disease, highlighting the importance of these activities in patient well-being. However, the same study noted that for individuals with a history of fractures light intensity activities might be more appropriate, highlighting the need for careful assessment from patient to patient.

Consequently, a fast, affordable and reliable prognosis tool is needed that can be easily integrated into clinical procedure. Computational simulations represent a promising approach, since they're non-invasive and can be performed patient-specifically. A modelling approach commonly used for the mechanical evaluation

of bone based on imaging data is the Finite Element Analysis (FEA) [78, 108, 27, 11]. However, current FE models usually simulate a simplified one-legged stance loading scenario and may therefore have limited ability to predict activity-specific fracture risk [23, 27, 94].

This thesis focusses on comparing the prediction of fracture risk during gait as one exemplary activity using two types of FE models: a physiological model and a simplified model. The physiological model aims to reproduce the actual loading and constraint conditions of the femur in situ during a full gait cycle. In contrast, the simplified model aims to reduce the extent of required input data and computation time, while maintaining comparable predictive performance. The objective is to evaluate whether simplified models can reliably assess fracture risk during walking, thus supporting better-informed clinical decisions.

1.2 State of the Art

1.2.1 Clinical

Metastatic bone disease frequently affects the axial and appendicular skeleton [21]. Tumor-induced bone destruction, particularly in lytic lesions, compromises structural integrity by promoting osteoclastic activity and suppressing bone formation [21, 63], significantly increasing fracture risk. Diagnosis and monitoring rely on imaging techniques, divided into structural methods such as radiographs, Computed Tomography (CT) or metabolic imaging approaches, such as Positron Emission Tomography (PET) [19]. Besides orthopaedic interventions, treatment strategies include radiotherapy, endocrine therapies, chemotherapy and pain management to control disease progression and reduce skeletal complications [19].

Traditionally, the clinical assessment of fracture risk in long bones relies on scoring systems based on lesion characteristics. The most widely used tool is Mirels score, introduced in 1989. It considers four criteria: lesion site, lesion type (lytic, mixed or blastic), pain level and the size of the lesion relative to the bone diameter. Each criterion gets a score from 1 to 3, resulting in a total score range of 4 to 12. A score of 9 or higher indicates a significant risk of fracture, advising surgical stabilization. [65]
While the Mirels score is widely used due to its simplicity and high sensitivity, it has limitations, including the subjectivity in pain assessment and moderate specificity, potentially leading to overtreatment [9].

An alternative approach employs cortical involvement measurements in predicting pathological fractures. *Van der Linden et al.* [61] demonstrated that axial cortical involvement (measured from conventional radiographs) exceeding 30 mm is associated with a significantly increased risk of fracture. The study reported a sensitivity of 86% and specificity of 58% for this threshold.
Similarly, *Tatar et al.* [99] found that a circumferential cortical involvement (measured via CT scans) greater than 30% significantly elevates fracture risk. The study reported a sensitivity of 100% and specificity of 89%, suggesting that CT-based measurements may provide more accurate support in clinical decision-making. However, the study was conducted retrospectively and on a relatively small population sample, lacking a broadly proven reliability.
Overall, comparing several of these conventional guidelines led to the conclusion they're still insufficient [11].

1.2.2 Preclinical

Finite element analysis (FEA) serves as a powerful preclinical tool by enabling detailed simulations of complex biological structures, allowing researchers to predict how these structures respond to various mechanical loads and conditions. This computational approach not only enhances our understanding of injury mechanisms and treatment outcomes but also aids in the design of more effective medical devices and interventions tailored to individual patient needs.

Mesh Generation Current FE models are typically patient-specific, constructed from Quantitative Computed Tomography (QCT) scans. The femoral geometry is discretized either into geometry-based tetrahedral meshes or into voxel-based hexahedral meshes. With tetrahedral meshes being more precise in representing the bone surface and allowing for local refinement around the lesion site, they are applied in studies where geometrical accuracy is superior to computational performance. Hexahedral meshes simplify the bone density-based material assignment substantially, since image voxels are directly translated to FE elements and allow for a high level of automation. However, a drawback is the stair-step approximation of bone surfaces, which can introduce artificial stress concentrations at the surface. Independent of the mesh type chosen, a high correlation ($R^2 \approx 0.9$) with experimental failure loads was shown. [86]

Material Modelling Bone tissue is typically modelled as a isotropic and linear-elastic [58, 94, 106], since the resolution of current clinical QCTs cannot account for anisotropy [86]. To determine the failure load of the whole bone despite using linear-elastic material, the results of the simulation are scaled until a certain failure

criterion is met. These failure criteria are often a stress- or strain-based element-wise threshold [58]. Linear-elastic models capture the onset of bone yielding but cannot simulate post-yield behaviour, often leading to an underestimation of the actual fracture load [86]. To address this, other FE models have been implemented using elasto-plastic material behaviour. Nonlinearity of the material is described using perfect plasticity with softening behaviour [57, 33, 7], a decrease of the Young's Modulus [44] or an elastic-damage constitutive law [10]. However, the incorporation of nonlinear material behaviour is computationally more demanding, emphasizing the importance of reducing the model complexity in other aspects.

Loading and Boundary Conditions A common simplification in the literature is to apply an axial load to the femoral head to mimic single-leg stance, while neglecting muscle forces. This approach is often combined with a cropped bone geometry, retaining only the proximal femur for analysis. The proximal femur is then constrained at its distal end either by pinning all nodes [98, 106, 27] or using high-stiffness springs [33]. While such simplified setups have been widely used and may improve general fracture risk assessment [18, 12, 27], their reliability for predicting activity-specific fracture risk in femora with metastatic lesions remains uncertain.

A first comparison between simplified and "physiological" loading and boundary conditions for femora with metastatic lesions was published by *Johnson et al.* [54]. The physiological boundary conditions during different activities were adapted from a previous study [92], but only a few muscle forces were included in the model. In addition, the analysis focussed exclusively on the time point of peak hip joint loading, which may not necessarily represent the point in time of highest fracture risk in bones with metastases. For instance, hip joint loads of lower magnitude but different direction, or muscle forces themselves, may lead to fracture prior to reaching peak hip joint load in the gait cycle.

Alternative approaches to conventional FEA CT-based Structural Rigidity Analysis (CTRA) represents an alternative to FEA, that estimates bone strength by computing axial, bending and torsional rigidity from CT scans. It models the femur as a beam and assesses whether the presence of the lesion reduces its structural rigidity beyond a critical threshold (approximately 35%) [28]. A study from *Damron et al.* [28] reported a sensitivity of 100% and a specificity of 60.6% for predicting impending pathological fractures with CTRA, considerably outperforming the Mirels score. While both approaches, FEA and CTRA showed a good correlation with experimental results, FE results tended to be slightly more accurate, while CTRA required less expertise in application [7].

Recent developments in machine learning have created new possibilities for

fracture risk assessment, offering a fast alternative with less inputs required, compared to conventional approaches. In this context, *Synek et al.* [97] introduced a hybrid method using Convolutional Neural Networks (CNN) to predict femoral strength based on 2D radiographic images. The networks were trained on paired datasets of 2D projections and corresponding strengths derived from FE simulations. The CNNs showed a high predictive performance, slightly inferior to current FE models. Aside from FE models, neural networks have great potential for clinical applicability due to their computational efficiency.

1.3 Thesis Goals

1.3.1 Gap

While FE-based methods have been applied to assess fracture risk in femora with metastatic lesions, they often yield abstract outputs, such as percentage-based risk scores (e.g. the Bone Strength (BOS) score [33]), which offer limited practical guidance for patients. To date, no activity-specific fracture risk assessment has been conducted, which would be potentially more helpful for patients.

As outlined in Section 1.2.2, previous FE models were used with simplifications regarding loading and geometry. However, the validity of these assumptions in the context of metastatic lesions and for specific activities of daily living remains uncertain. Although physiological FE models are more detailed, they can be too time-consuming for routine clinical use. Therefore, it is of interest to evaluate whether simplified models are sufficient to predict activity-specific fracture risk. One study by *Johnson et al.* [54] addressed this by comparing simplified and physiological FE models for femora with metastatic lesions, but neglected the time course of muscle forces during activities.

1.3.2 Objectives

A detailed, activity-specific fracture risk assessment tool for a femur with an arbitrary metastatic lesion is still missing. This thesis aimed to fill this gap based on two objectives:

(1) **Developing a physiological FE model** for femoral fracture risk assessment considering the entire time course of an activity, including muscle and hip joint forces, for a femur with an arbitrary metastatic lesion. The activity "walking" is chosen as an exemplary activity.

(2) **Comparison of the physiological FE model with a simplified model**, which assumes simplified loading and geometry. This comparison is performed on a larger number of artificial lytic lesions and should reveal, if the effort of creating a physiological FE model is warranted.

2 Theoretical Background

2.1 Bone Mechanics

Bone is a composite biological material with a hierarchical structure. The bone Extracellular Matrix (ECM) is composed of approximately 70 % inorganic mineral (primarily hydroxyapatite), 20 % organic (mostly type 1 collagen) and 10 % water and trace components [35, 26]. This composition combined with its structural organization gives bone its essential mechanical properties, stiffness and toughness [26], enabling functions such as structural support and protection, providing a framework for motion and serving as a calcium reservoir [35].

Properties of Cortical and Trabecular Bone
At the macrostructural level, bone tissue is classified into two types: cortical (compact) bone and trabecular (cancellous) bone, both illustrated in Fig. 1. Cortical bone forms the dense outer shell of bones and is characterized by low porosity, whereas trabecular bone forms the highly porous internal structure. On the microscopic level, cortical bone is organized into osteons (cylindrical lamellar structures) surrounded by circumferential lamellae. In contrast, trabecular bone consists of a 3D network of interconnected struts called trabeculae, with the intervening spaces filled by bone marrow. [35]

Due to its higher volume fraction of mineralized matrix, cortical bone is much stiffer and stronger than trabecular bone. Cortical bone has a Young's modulus of approximately 17–22 GPa [82, 77] in longitudinal direction and exhibits a compressive strength of 150–200 MPa [68]. In contrast, the apparent elastic modulus and the compressive strength of trabecular bone is considerably lower and is highly dependent on density and architecture [35]. Notably, the apparent mechanical properties of both bone types are strongly density-dependent: experimental studies have shown compressive strength scales approximately with the square of apparent density [16], a relationship that applies to both cortical and trabecular bone [16].

Cortical bone demonstrates anisotropic mechanical behavior due to the longitudinal alignment of osteonal structures and the lamellae orientation in the

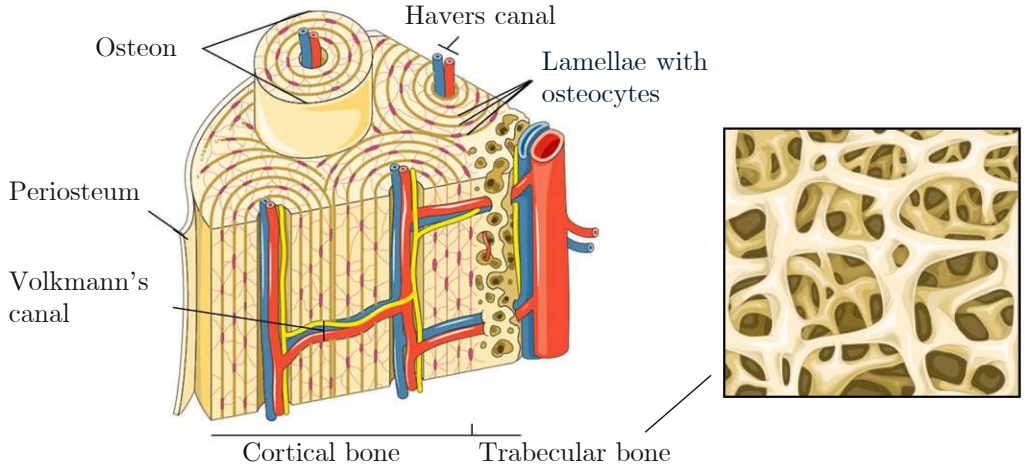

Figure 1: Structural organization of cortical bone (left) and trabecular bone (right) (adapted from [104]).

bone. This anisotropy results in a higher stiffness and strength under axial (longitudinal) loading compared to transverse loading. [35] Considering the usual loading of bone, it makes sense that bone is stronger in compression than tension [77]. The structural adaptation of bone to its loading conditions (often referred to as "Wolff's law"), is further reflected by the alignment inside trabecular bone (Fig. 2). As a result, the trabeculae are often aligned along principal stress trajectories [82] to enhance strength [95].

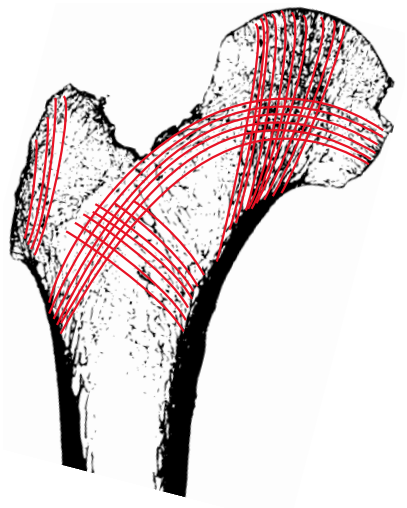

Figure 2: Schematic illustration of the load-adapted trabecular bone structure in the proximal femur.

Anatomy and muscle insertions of the femur

The femur is the largest long bone in the human body, illustrated in Fig. 3. The diaphysis, also called femoral shaft, is bordered by the proximal and distal epiphyses of the bone. At the proximal end, the pyramid-shaped neck connects the spherical femoral head with the cylindrical beginning of the diaphysis [43]. At the transition area between neck and shaft are two characteristic bony protrusions, namely the greater and lesser trochanter [43]. Distally, the femoral diaphysis broadens into a cuboidal base with the medial and lateral condyles [43].

Bone morphology changes from a porous trabecular structure surrounded by a thin cortical shell at the proximal and distal end of the femur, to a thicker hollow cortical structure in the shaft [52].

The insertion areas of the main muscles acting on the femur are also labelled in Fig. 3.

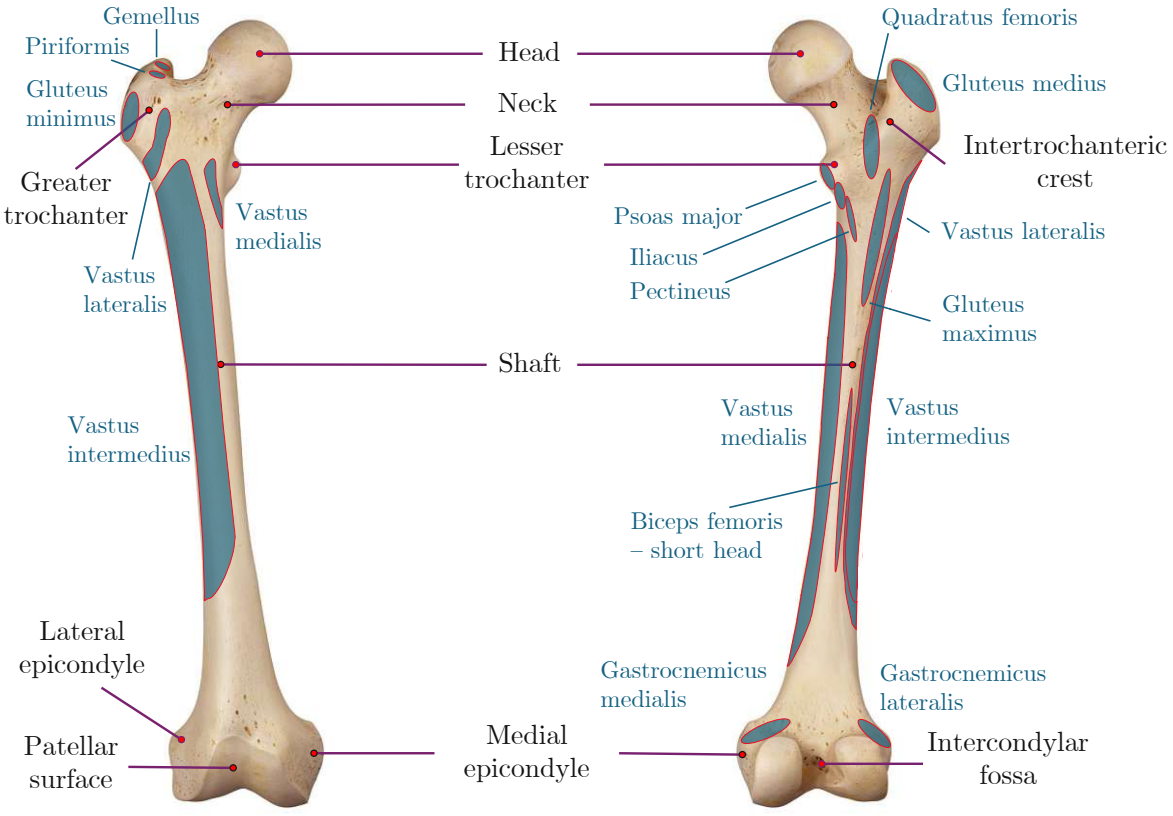

Figure 3: Anatomy of the femoral bone with characteristic morphologies and muscle insertion areas (adapted from stock.adobe.com, [45]).

2.2 Metastatic bone disease

Bone tumours occur in two forms in the skeleton: as primary or secondary (metastatic) tumours. Primary tumours arise in the bone itself, while metastases arise from cancer cells of other malignancies in the body that are distributed through the bloodstream. Bone metastases are far more common than primary malignant bone tumours (e.g. 0.2 % of all malignancies in Italy and the United States reported in both genders) [39].

Metastatic bone disease is commonly associated with cancers of the prostate, breast, lung, and kidney. These malignancies typically metastasize to the axial skeleton and, in long bones preferentially to the proximal part. Bone metastases can appear as osteolytic, osteoblastic or mixed lesions. This classification is based on radiographic appearance: lytic lesions promote bone resorption by enhanced osteoclast activity, while blastic lesions promote sclerosis of the bone tissue by enhanced osteoblast activity. [21]
Lesion size varies by tumour type. According to the Mirels score, lesions occupying less than one-third of the bone diameter are considered mild, up to two-thirds moderate, and more than two-thirds severe [65].

Blastic lesions appear radiographically as dense, opaque spots (brighter than normal bone) due to excess mineralized tissue [63]. They are typically present in prostate cancer and small cell lung cancer, and may also occur in breast cancer [63, 21]. Blastic lesions are characterised by an uncontrolled growth of bone, although with inferior mechanical properties [93]. The cause for these inferior mechanical properties may be the unstructured nature of the new bone [93].

In contrast, lytic lesions appear radiographically as dark spots due to resorption of mineralised bone. They are typically present in breast cancer, multiple myeloma, non-small cell lung cancer and renal cancer [21, 63]. Their appearance depends on the primary tumour. For example, multiple myeloma metastases are characterised by a sharp, spheroid appearance with smooth borders and erased trabecular structure [84]. In contrast, metastatic lesions originating from breast cancer are characterised by round or oval lesions with denticulated margins and porous surrounding bone [13].

2.3 Finite Element Analysis

The FEA is a numerical method widely used to approximate solutions to differential equations, particularly for problems in structural mechanics where analytical solutions are not feasible. The core idea of FEA is to discretise a complex, continuous domain into a finite number of smaller, simpler sub-domains, called finite elements, over which the solution is approximated. As the number of elements increases, the computed solution is expected to converge towards the true continuum solution. [70]

Finite elements can differ in dimensionality and characteristics. Typical examples include beam elements for one-dimensional structures, shell elements for thin two-dimensional structures or solid elements for three-dimensional volumes. The elements are interconnected through so called nodes, collectively forming the FE mesh that discretely represents the complex domain. [77]

In the context of solid mechanics, the governing equations describe the deformation of a body under applied boundary conditions, while accounting for the material's constitutive behaviour. The fundamental assumption underlying the solution is that of static equilibrium.

In more detail, each node of an element can be subjected to either essential (geometrical) or natural (force) boundary conditions and each element's mechanical behaviour is characterized by a local stiffness matrix. This element stiffness matrix relates nodal forces with nodal displacement and can be computed using the material stiffness matrix and shape functions, which interpolate the displacement field within the element. [77]

By assembling the contributions of all individual elements, stiffness matrices and boundary conditions, a global system of linear equations is established. This global system follows the general form:

$$\mathbf{KU} = \mathbf{F} \tag{2.1}$$

where $\mathbf{K}$ is the global stiffness matrix, $\mathbf{U}$ is the vector of nodal displacements, and $\mathbf{F}$ represents the vector of applied boundary conditions. [77]

Mesh Types

In solid mechanics, the most commonly used element types for 3D analyses are hexahedral (brick-shaped) and tetrahedral (pyramid-shaped) elements [1]. Generally, finer discretizations (more and smaller elements) improves the solution accuracy, although at the expense of higher computational cost [85]. Thus, a well-designed mesh is crucial to achieve an acceptable trade-off between accuracy and computation time.

Since automated meshing and computational efficiency are particularly important in the present application, a specific subclass of hexahedral meshes, called "voxel-based meshes" is particularly suitable. Voxel-based meshes are commonly used for modelling bone from CT data [57, 34, 11]. Given that CT scans consist of voxels (volumetric pixels), voxel-based meshing directly converts each image voxel into a hexahedral element, with material properties assigned based on local bone density (Fig. 4) [78, 10].

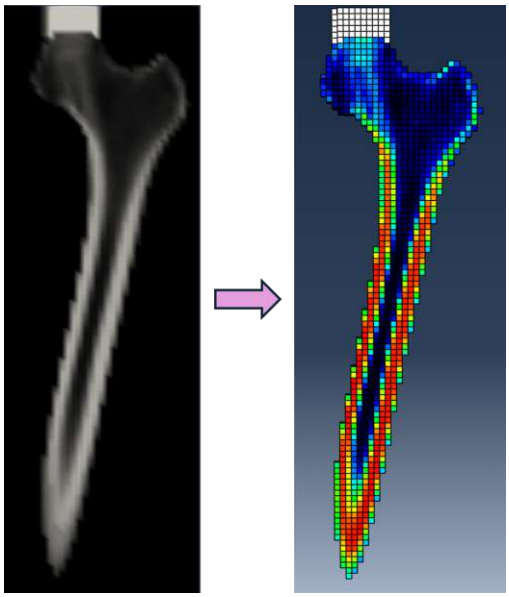

Figure 4: Direct conversion of image voxels into hexahedral FE elements.

A key advantage of this approach is its high degree of automation, which allows for mesh generation without the risk of poor quality or distorted elements, regardless of the complexity of the geometry [87]. Voxel-based meshes are therefore straightforward to generate. However, they also have limitations. Due to their brick geometry, voxel meshes produce stair-step approximations of curved surfaces, which can introduce artificial stresses at the model surface [87]. In addition, voxel meshes lack local refinement at failure sites that would be beneficial [34].

Material Mapping

Besides the FE mesh generation, a key step in CT-based FEA of bone is the assignment of appropriate mechanical properties to the elements based on the gray scale of the CT scan. The gray scale (reported in Hounsfield Units) quantifies the local radiodensity of the scanned tissue, which for bone, reflects the mineral content [31].

In homogenized FE models, each CT scan voxel is associated with a single radiodensity, representing an averaged property of the bone–marrow mixture within that voxel. Homogenization refers to this averaging process and the determination of the resulting apparent material properties. [34])

By using calibration phantoms with known densities, a conversion relationship is established between Hounsfield Units and Bone Mineral Density (BMD) [77]. Subsequently, empirical relationships are applied to estimate mechanical properties, such as stiffness or strength from the BMD [77]. Typically, these relations take the form of a power law [48], such as the following for the elastic modulus E:

$$E = E_0 \cdot BMD^k \tag{2.2}$$

In the above power law, E_0 and k are calibration constants, and BMD is taken from a specific voxel of the CT image to compute the elastic modulus E.

Another important aspect of material mapping in FEA is anisotropy. Both trabecular and cortical bone exhibit anisotropic behaviour [51, 68]. To model the morphology and resulting anisotropy of trabecular bone in FEA, researchers have developed an approach where a fabric tensor is computed from the bone's microstructure (using techniques like the Mean Intercept Length (MIL) [77]) that characterizes the orientation and degree of anisotropy [107, 78]. Anisotropic stiffness tensors and failure criteria can then be defined based on the fabric tensor. For instance, *Zysset and Curnier* [107] proposed an orthotropic elasticity model based on fabric tensors combined with a density-dependent power law relationship.

However, many CT-based FE studies continue to model bone as isotropic, using density-dependent power law relationships, since the clinical resolution of QCT scans is insufficient to capture trabecular morphology [78]. The impact of including anisotropy remains an active area of research: while some studies found little difference in outcome between assuming isotropic versus orthotropic material properties in femur FE models [80], others reported significant changes in predicted bone strengths when anisotropy was considered [62, 79].

Modelling metastatic lesions

The challenge of incorporating metastatic lesions into a FE model, is to modify the bone's geometry and material properties locally to reflect the presence of the tumor-induced damage.

Previous studies have shown that FE models represent the structural mechanical properties of bones accurately without applying an explicit material model for the metastatic lesion [93, 57]. However, *Kaneko et al.* [56] reported that cortical bone affected by metastatic lesions had a lower elastic modulus and compressive

strength than its density suggested, when comparing it to healthy bone. That would alter the applied bone mineral density–stiffness relationship.

Regarding the geometric representation of osteolytic lesions, a common approach is to model osteolytic lesions as a void in the bone either in a computational or experimental context [11, 32], assuming negligible mechanical properties of the lesion. While this is a suitable approach for lytic lesions, it is not applicable for ostoblastic lesions, in which case it might be necessary to introduce another material model for the tumour tissue.

2.4 Musculoskeletal Modelling

Musculoskeletal modelling is a computational approach to investigate the interaction of muscle forces and movements of a body [30]. The basic prerequisite for this is a model to represent the physiology and anatomy of a musculoskeletal system with all its components. Combining this with the mechanical principles of multi-body or multi-joint dynamics allows the simulation of a movement. With this theoretical framework, the influence of neuromuscular excitation patterns on muscle forces and body movements can be investigated, properties that cannot be easily measured in vivo. [30]

In a musculoskeletal model, each bone is typically represented as a rigid body with certain mass and inertial properties. The model's joints define the kinematic relationship between these bodies. Additionally, musculotendon actuators are included in the model to generate forces dependent on anatomical parameters. [74, 59]

The principle of musculoskeletal modelling is based on Newtonian mechanics [89, 4]. Each body segment is treated as a rigid body subjected to external forces (e.g. ground reaction forces) and internal forces (muscle and ligament forces). The resulting equations of motion describe how the applied forces generate accelerations of the respective body segments [89, 4].

As already mentioned, musculotendon actuators are implemented in a musculoskeletal model to represent the actions of muscles. Typically, a Hill-type muscle model is used. This type of model includes several elements arranged in parallel and series, accounting for the development of muscle force that varies nonlinearly with the muscle length and the contraction velocity, as well as passive forces resulting from stretching tendon and muscle tissue [64]. Specifically, muscle force is determined by three factors: the activation level

(ranging from 0 (no contraction) and 1 (full contraction)), the normalized length of the muscle unit and the normalized velocity of the muscle unit [76].

Dynamic simulations in musculoskeletal modelling can be conducted either using a forward or an inverse approach. The corresponding steps involved in the process are illustrated in Fig. 5.

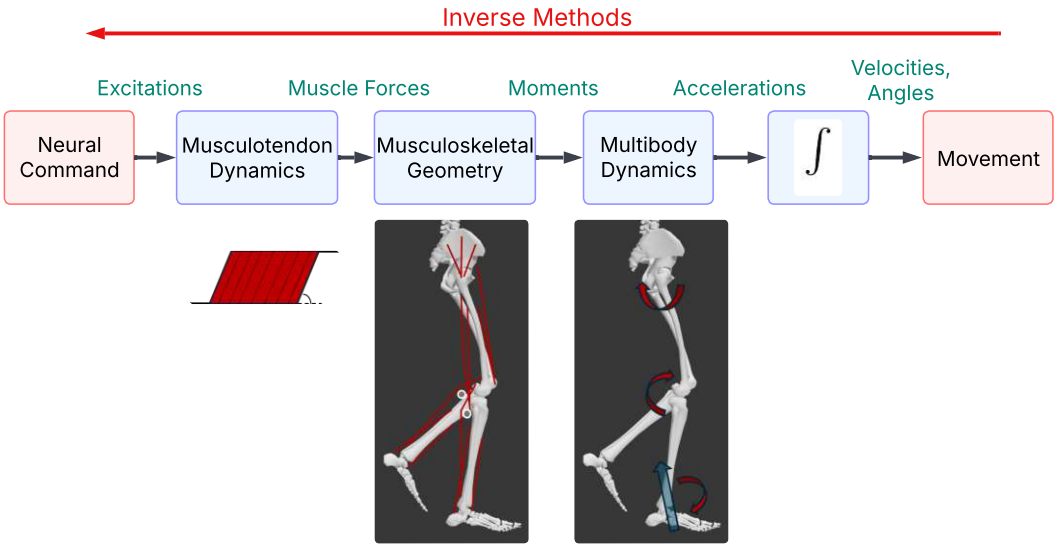

Figure 5: Steps comprised in a musculoskeletal simulation: from neural excitation via muscular and skeletal properties to the resulting movement of the model (adapted from [90]).

Inverse Problem: Inverse methods take measured kinematic data (e.g. joint angles, displacements, velocities) and external forces as inputs to compute the net joint moments required to reproduce the observed motion with the given musculoskeletal model. Because multiple muscle force combinations can satisfy a given joint moment (also called "the muscle redundancy problem"), optimization techniques are applied to determine a physiologically plausible solution. A major advantage of the inverse approach is its higher computational efficiency compared to forward dynamics simulations [37].

Forward Problem: Forward methods, by contrast, start with the neural commands, which are first transformed into muscle excitations and, based on musculoskeletal dynamics and geometry, ultimately result in muscle forces and joint moments [14]. Joint moments are then translated into joint movements through the equations of motion, as shown in Fig. 5. While forward methods are not confronted with the muscle redundancy problem [14], they are more complex and computationally demanding [37].

3 Methodology

This chapter outlines the methods used, beginning with the study design to provide an understanding of the overall workflow. Subsequently, the two modelling approaches under investigation are explained in detail, including associated processing steps. For the physiological model, this includes the combination of musculoskeletal modelling with FEA. The models were applied to a large sample of femora with artificial lytic lesions and the femora were classified as fractured or non-fractured based on a simplified failure criterion. The chapter concludes with a description of the criteria according to which the overall model results are compared.

3.1 Study Design

This study was based on a hip CT scan of a single individual. Artificial metastases were incorporated into the scan, resulting in a sample of 93 bones with metastatic lesions having varying characteristics. In case of the physiological model, those bones were then used to simulate a whole gait cycle including all muscle forces and the hip joint load acting on the femur, as computed by a musculoskeletal model. In contrast, only the moment of peak hip joint load was simulated for the simplified model. Based on a simple failure criterion to classify bones as fractured or non-fractured, a confusion matrix could be determined characterizing the prediction results of both models and their comparison. The process is illustrated in Fig. 6.

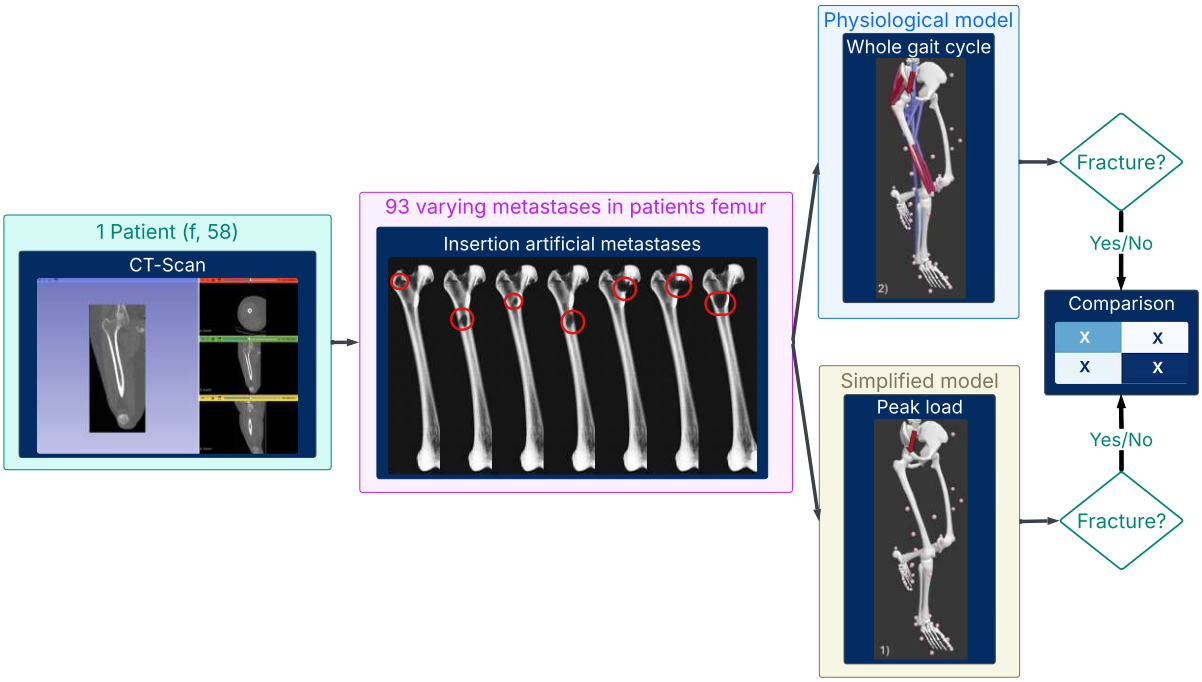

Figure 6: Study Design: Insertion of metastatic lesions into the patient's CT scan, followed by fracture risk assessment with both modelling approaches.

3.2 Musculoskeletal Model

Due to the absence of patient-specific kinematic data recorded during walking, in combination with a femoral CT scan from the same individual, it was necessary to use a generic musculoskeletal model. This model needed to be both scalable to the patient's anthropometric characteristics and has publicly available kinematic data.
The open-source software *OpenSim* (SimTK, Stanford University, Stanford, USA) was selected as the simulation software. Among its core models, the "Gait2392"-Model was chosen. This decision was primarily based on the model's widespread use and validation in the literature, which ensures a reliable basis for contextualizing and comparing results [83, 55, 25].

The following detailed model description is taken from the *OpenSim* documentation [100]. The Gait2392-Model is a three-dimensional, 23 Degrees of Freedom (DoF) lower-extremity model with 92 musculotendon actuators representing 76 muscles [100]. It is composed of seven body segments (pelvis,

femur, tibia, patella, talus, calcanus, toe) per body half, each with its own reference frame, as shown in Fig.7. The bone geometries and anatomical data were adapted from several studies [40, 49, 103, 96, 50, 15]. The body segments are connected via five joints (hip, knee, ankle, subtalar, metatarsophalangeal) to describe their relative motions. The joint definitions featured in the model were adapted from [29], with an extended version of the knee model from [105].

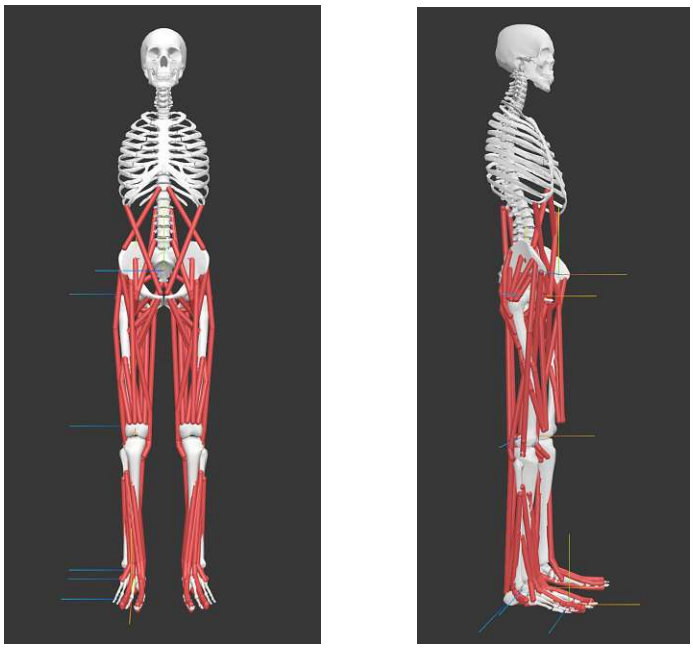

Figure 7: Musculoskeletal model Gait2392 in anterior- and lateral view.

Muscle paths are constituted by line segments from origin to insertion landmarks, incorporating intermediate points if necessary to represent wrapping geometries. Peak isometric forces of the muscles were also adapted from [29], however muscle strengths were rescaled in order to better match experimental results from healthy, living subjects. Optimal fiber length and pennation angles for the muscles were taken from [103]. Anthropometric data from 5 subjects (age: 26 ± 3 y, height: 1.77 ± 0.03 m, weight: 70.1 ± 7.8 kg) was used to define mass and inertial properties for the body segments, following the approach of [5], with an additional scaling factor of 1.056 for the inertial properties. The unscaled version of the model represents a subject that is 1.80 m tall with a weight of 75.16 kg. No marker sets are associated with it.
The experimental data provided with the musculoskeletal model was collected with a data collection protocol identical to that described in [53], although the

subjects differed. The available experimental data from *OpenSim* corresponds to a subject with a height of 1.80 m and a weight of 72.6 kg.
Data was recorded during treadmill walking at a predefined speed of 1.36 $\frac{\text{m}}{\text{s}}$ on a treadmill (Bertec Corporation, Columbus, OH, USA) with one split belt assigned to each foot. The moment and force exerted by each foot on the treadmill was measured by a force plate under each split belt every $\frac{1}{600}$s. A six-camera system (Motion Analysis Corporation, Santa Rosa, CA, USA) was used to track the positions of 49 reflective markers, that were attached to the subject, every $\frac{1}{60}$s. [53]

3.3 Computed Tomography Scan

The CT scan used in this thesis is part of the *Hip-Fracture Valid Collection* [2], a dataset composed of calibrated CT scans of whole femora with their corresponding segmentations. For a more detailed description of the dataset refer to the corresponding manual [2].

The subject selected for this study had to match the body height of the experimental subject of the Gait2392 model (1.80 m) due to the lack of motion capture data. Therefore, the scan of an 58-year old female with a body height of 1.80 m and a body weight of 88 kg was selected. No fracture occurred in either of the femora prior to arthroplasty. For this study, the right femur was chosen. Both, the Stereolithography (STL) file and the CT scan of the chosen femur are visualized in Fig. 8.

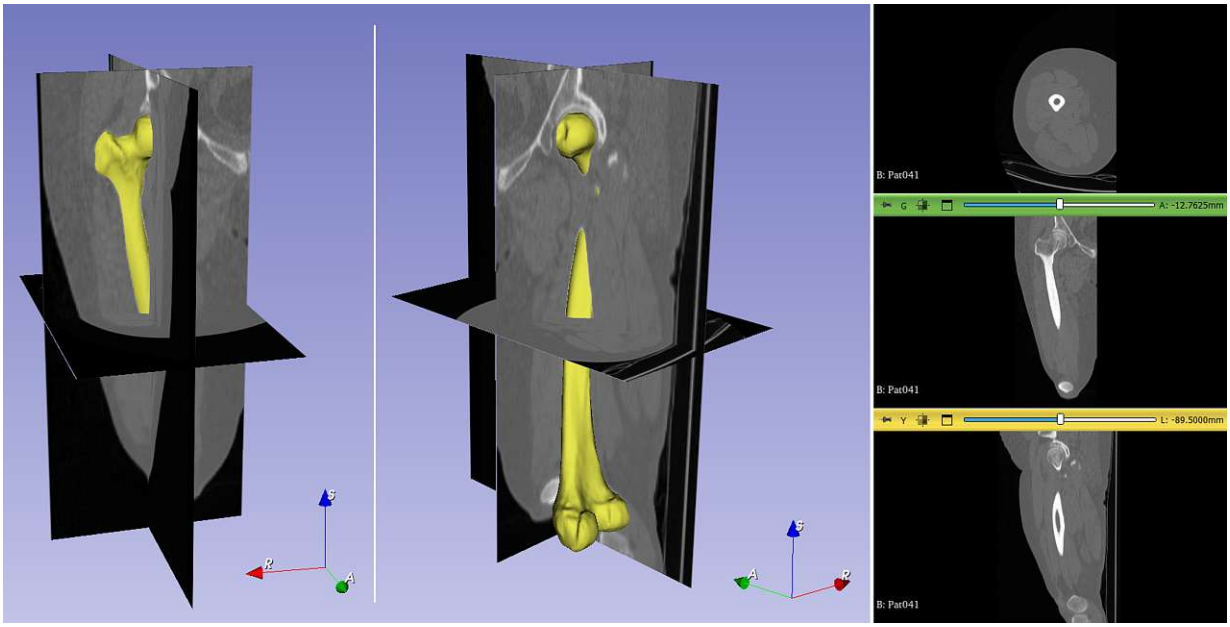

Figure 8: 3D views of the CT scan with the segmented femoral bone (yellow).

3.4 Insertion of Artificial Metastatic Lesions

Artificial metastatic lesions were inserted into the CT scan of the femur as described in a previous study [97]. In brief, lytic lesions were simulated by attenuating the local bone density within randomly located, sized and oriented ellipsoids. The bone density was exponentially decreased from the original value at the ellipsoid boundary towards zero at the ellipsoid centroid. The generation of lesions was limited to the proximal third of the femur. The largest semi-axis of each ellipsoid was randomly selected within a range of 10 mm to 30 mm. The two remaining semi-axes were defined by a random ratio in the range of 0.4 to 0.6 with respect to the largest semi-axis. Using this approach, 914 variations of the femur, each containing a different single lytic lesion, were created. Exemplary lesions are illustrated in Fig. 9.

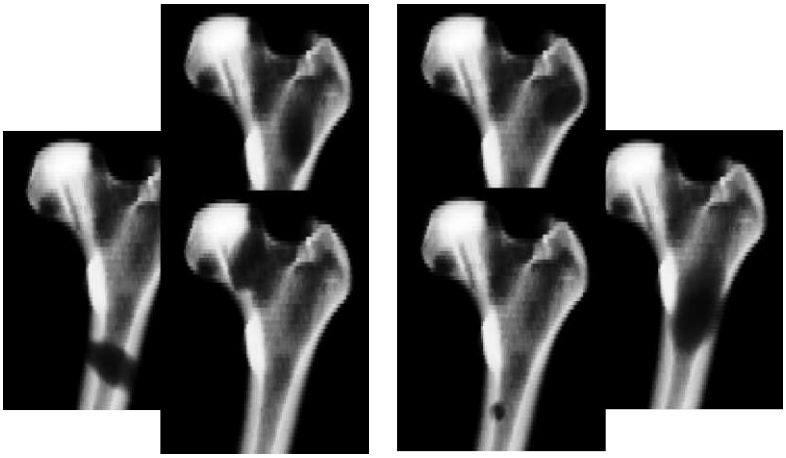

Figure 9: Exemplary metastatic lesions shown in femoral projections.

3.5 Physiological Model

The workflow for the physiological model, illustrated in Fig. 10, constituted a central aspect of this thesis. The steps required for its implementation are shortly described in the following.

After choosing the musculoskeletal model Gait2392, acquiring the CT scan and inserting artificial metastases, the simulation of a full gait cycle was performed using *OpenSim*. Following the principle of inverse problem solving, a series of steps were carried out to determine the muscle attachment sites, the muscle forces acting on the femur and the hip joint load.

To relate the simulation results to the actual bone geometry of the patient, the generic femoral geometry distributed with *OpenSim* was registered to the segmented patient femur from the *Hip-Fracture Valid Collection* [2] using surface registration. Therefore, the *CMF* extension of the open-source software *3DSlicer* [36] was used. *3DSlicer* is typically used for visualizing, processing and registering 3D-Images and meshes.

Separately, the CT scan of the patient was processed using *Medtool* (Dr. Pahr Ingenieurs e.U., Pfaffstätten, Austria), a script management tool specialized in processing CT- and Magnetic Resonance Imaging (MRI) data. Image processing comprised steps such as converting Hounsfield Units to bone mineral density, cropping the image, and adding an embedding.

Based on the resulting geometry and bone mineral density information derived from the CT scan, along with the customized load data from *OpenSim* an FE model was built in *Abaqus* (Dassault Systèmes, Vélizy-Villacoublay, France). *Abaqus* is a software for finite element analyses covering a wide range of application fields.

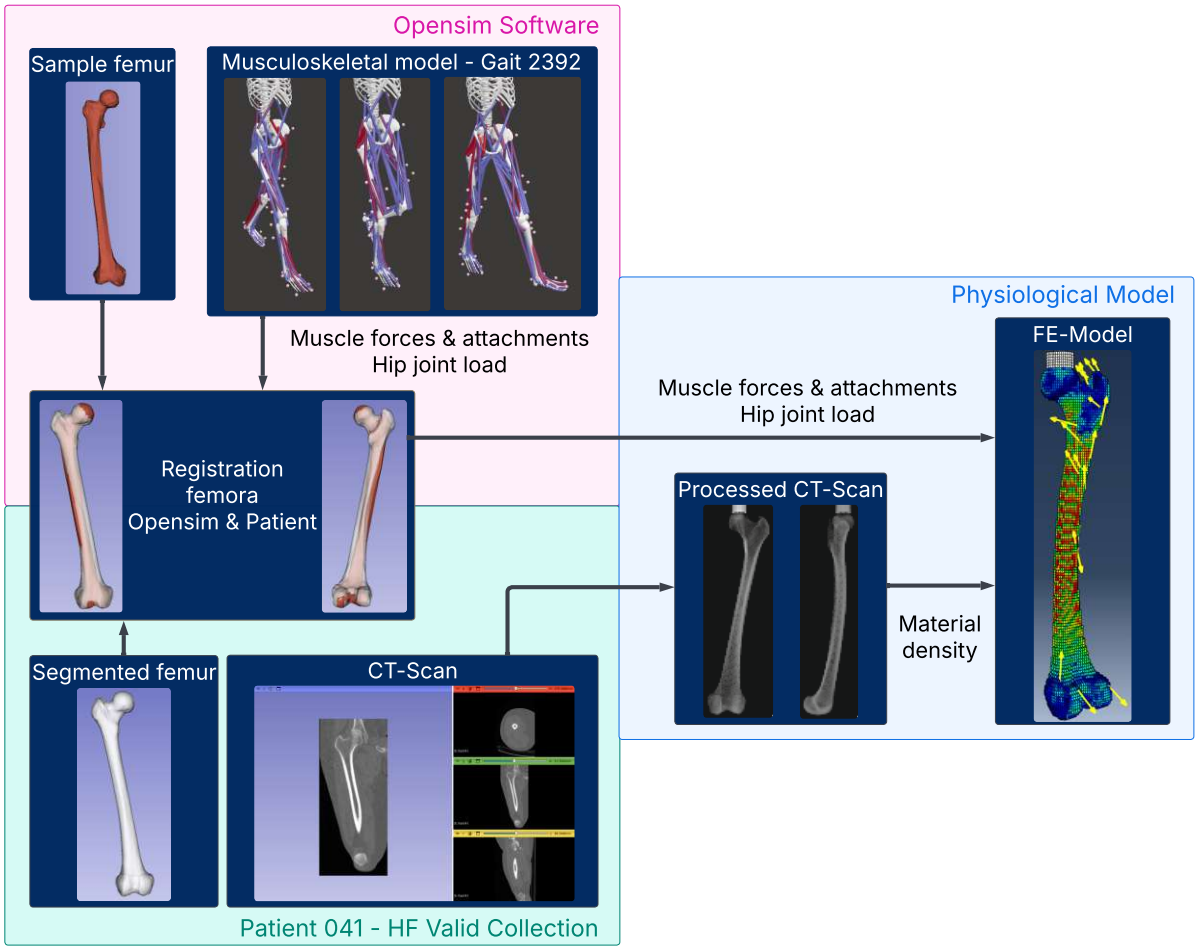

Figure 10: Workflow for the physiological model.

3.5.1 Musculoskeletal Modelling

Since the musculoskeletal model and patient for the study were fixed as inputs, the musculoskeletal simulation of the gait cycle was conducted next.
The gait cycle simulation comprised several steps. First, the generic Gait2392-Model was scaled to the anthropometric data of the subject for whom

movement and ground reaction forces had been recorded, as described in Section 3.2. Subsequently, the model motion that best matched the experimental marker trajectories was determined using the Inverse Kinematics (IK) tool in *OpenSim*. Residuals resulting from dynamic inconsistencies were minimized using the Reduced Residual Algorithm (RRA) tool. Subsequently, Static Optimization (SO) was performed to estimate individual muscle forces based on the calculated net joint moments. The Joint Reaction Analysis (JRA) tool was then used to determine the hip joint forces, and the Muscle-Force-Direction (MFD) plugin was included to extract muscle attachment coordinates and muscle lines of action [81, 8].
All these steps were governed by setup files, which specify the conditions under which procedures are executed in *OpenSim*. Setup files for several steps were provided with the software and were either directly adopted or slightly modified. The modifications made are described in the following sections. Further details on scaling, IK, RRA, SO, JRA and the MFD plugin are also provided below.

3.5.1.1 Scaling

As mentioned in Section 3.2, the generic version of the model represents a subject with a height of 1.80 m and a weight of 75.16 kg, without an associated marker set. To conduct the gait analysis, the model was scaled to match the size of the subject with available motion capture recording (height: 1.80 m).
During the scaling procedure, a virtual marker set was assigned to the generic model, representing the default joint configuration. With a static trial containing experimental marker trajectories, the virtual markers were aligned to best match the experimental markers, thus scaling the generic model segment lengths. The extent to which virtual markers were allowed to deviate from experimental markers, was defined by marker and coordinate weights, adopted from the *OpenSim* example data. Additionally, femur and tibia were manually scaled with a uniform factor across all three dimensions, adopted as well from *OpenSim* example data. Geometrical properties such as muscle path points were automatically scaled with segment geometry, whereas muscle strengths remained unchanged. [75]

In the same process, the model was scaled to match the body weight of the selected patient from the *Hip-Fracture Valid Collection* [2] (weight: 88 kg). Segment masses of the musculoskeletal model were first scaled by their individual length scale factors and then adjusted to constitute the new target total mass, while preserving relative segmental mass distribution [75]. Since the model weight was scaled, the ground reaction forces from the experimental data had to be scaled as well. The ratio of target to original model mass was used for this purpose.

3.5.1.2 Inverse Kinematics

After scaling the model, the IK algorithm was applied using a walking trial instead of the previous static trial. The walking trial consisted of the experimental data described in Section 3.2, that comprised several seconds of 49 marker trajectories recorded from a subject walking on a treadmill with a velocity of $1.36\frac{m}{s}$.

The IK algorithm adjusts the pose of the scaled model for each time frame targeting the best possible match with the recorded marker trajectories. The objective hereby is to minimize the sum of the weighted squared errors between the experimental marker data and the corresponding points on the model [71].

3.5.1.3 Residual Reduction Algorithm

Although the kinematic data of the experimental subject was recorded consistently and simultaneously with the ground reaction forces, large non-physical compensatory forces at the pelvis [72], also called residuals, were required to satisfy the force equilibrium equations. These can result from simplifications in modelling or marker data processing. The RRA can be used to minimize such residuals. To achieve this, the RRA can slightly adjust the segment Center of Mass (CoM), segment masses and/or kinematics [72].

The adjustment of the CoM is performed automatically by the RRA. Since suggested segment mass changes are not applied automatically, a custom Python script was implemented. After updating the CoM, the RRA reiterates the tracked motion and adjusts the kinematics to reflect the altered CoM [72].

3.5.1.4 Static Optimization

With the adjusted musculoskeletal model, kinematic data and minimized residuals, a SO was performed. SO is an extension of the Inverse Dynamics (ID)-Method, which was performed first. ID analysis uses the equations of motion to compute net joint forces and moments required to agree with given kinematics and external loads [73].

Despite knowing the net joint torques, the muscle redundancy problem remained, meaning that multiple muscle activation patterns could lead to the same joint moment. SO addresses this by minimizing a cost function, precisely the sum of squared muscle activations, to get individual muscle forces [73]. In the process, the muscle force-length-velocity relation was taken into account. The SO output comprised time-resolved individual muscle activations and - forces throughout the gait cycle.

3.5.1.5 Joint Reaction Analysis

Following the estimation of muscle forces, the resultant joint forces and moments, accounting for all motions and loads within the model, still were to be determined. For this purpose, the JRA tool in *OpenSim* was used [101].

Given that the joint concerned in this case, the hip, is modelled as a ball-and-socket joint, it does not transmit moments. Thus, only the resultant forces exerted from the pelvis to the femur were computed, expressed in the local femur reference system.

3.5.1.6 Muscle-Force-Direction Analysis

To actually apply the computed muscle forces to the FE model later on, the muscle lines of action and their attachment points on the bone had to be determined. Since there is no pre-installed functionality available for that in the *OpenSim* software, the external MFD plugin [81, 8] was integrated into the workflow.

An exemplary application of the plugin on the right femur is shown in Fig. 11. The user first specifies a target segment of the musculoskeletal model, upon which the plugin identifies all muscles attached to that segment. For each of them, the muscle path is extracted. The plugin provides two options for extracting muscle attachments and their force direction: anatomical and effective.

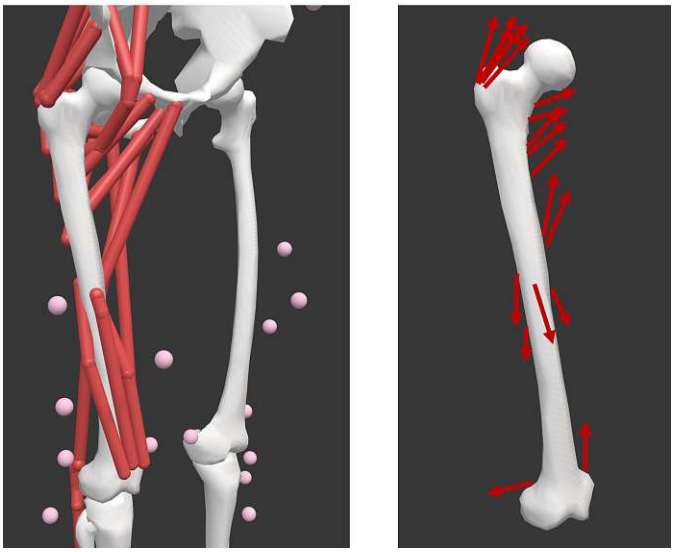

Figure 11: Exemplary application of the MFD plugin on the right femur.

Anatomical attachments refer to the locations where muscles are directly connected to the bone. However, if there are via-points or wrapping surfaces involved, the associated muscle force direction may not be represent the mechanical effect of that muscle on the segment (*MFD-Manual*, [67]). Therefore, the user can choose between anatomical and effective mode of extraction. The issue is illustrated in Fig. 12.

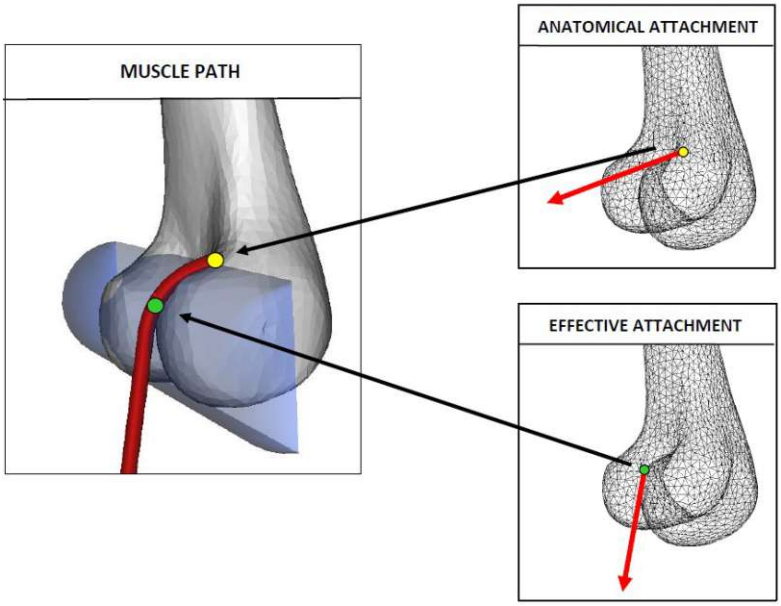

Figure 12: Possible muscle attachment extractions with the MFD plugin [81, 8, 67] for the Gastrocnemicus Medialis-Muscle (from [67]).

3.5.2 Transformation of Muscle and Hip Joint Forces

After completing the simulations with the Gait2392 model, the required musculoskeletal data was available. However, the obtained data corresponded to a scaled femur geometry derived from the Gait2392 model, rather than the chosen patient's actual femoral geometry from the *Hip-Fracture Valid Collection* [2]. Therefore, a registration of the Gait2392 model femur geometry onto the patients femoral geometry was necessary. As briefly mentioned in Section 3.5, this was done in *3DSlicer* with a semi-automatic surface registration tool of the *CMF*-Extension.

The unscaled femoral geometry from the Gait2392 model was exported and manually scaled using the software *VTK* (Kitware Inc., Clifton Park, NY, USA), according to the scaling procedure from *OpenSim* described above. Once the

geometry was scaled, it was imported into *3DSlicer* together with the patient's femoral geometry. An arbitrary positioning in space and limited similarity in terms of surface shapes could be observed between the femoral bones.

To overcome these inequalities, a surface registration was performed twice, based on the Iterative Closest Point (ICP) algorithm. The ICP algorithm is a standard approach in surface registration when it comes to aligning surfaces that are partially overlapping [66, 17]. It was applied twice because for a precise final surface alignment a rough pre-registration has to take place.

The ICP algorithm works by finding the closest point on a target surface for each point on the source surface and calculating the necessary transformation matrix for the whole point cloud (translation and rotation) to minimize the distance between the point pair. This process repeats iteratively for all points on the two surfaces until a convergence criterion is reached [41].

The surface registration tool of the *CMF* extension in *3DSlicer* provides three transformation options for aligning geometries: rigid-, similarity- and affine transformation. Given that surface geometries in this case varied significantly in both shape and size, as well as their initial spatial positioning, a single registration procedure was insufficient.
Therefore, the registration was performed in two stages:

1. A coarse **pre-registration** using **rigid transformation** for a rough alignment
2. A **refined registration** using **similarity transformation** for a precise result

For the second registration step, a choice had to be made between similarity and affine transformation. Affine transformation, which permits independent scaling along the three axes was ruled out, as it could lead to a distortion of the bone geometry by altering its proportions. In contrast, similarity transformation preserves the proportions of the bone geometry by allowing just one scaling factor along the three axes. However, it requires that the surfaces are already in proximity to each other and properly oriented.

Both registration procedures were performed using the absolute value as the mean distance mode, with a maximum of 2000 iterations, 200 landmarks and a maximum distance threshold of 0.001 mm. The registration procedures resulted in a two 4×4 transformation matrices operating on homogeneous vectors.

Rigid Transformation Matrix A rigid transformation consists solely of rotation and translation, without any scaling. The general form is as follows:

$$\mathbf{T}_{\text{rigid}} = \begin{bmatrix} \mathbf{R} & \mathbf{t} \\ 0 & 1 \end{bmatrix} = \begin{bmatrix} r_{11} & r_{12} & r_{13} & t_1 \\ r_{21} & r_{22} & r_{23} & t_2 \\ r_{31} & r_{32} & r_{33} & t_3 \\ 0 & 0 & 0 & 1 \end{bmatrix} \tag{3.1}$$

where r_{ij} represent the components of the rotation matrix and t_i the translation components.

The rigid transformation matrix obtained from *3DSlicer* with the translation component given in m was:

$$\mathbf{T}_{\text{rigid}} = \begin{bmatrix} 0.141665 & -0.0703832 & 0.987409 & 0.0833987 \\ -0.979614 & -0.15349 & 0.129606 & -0.00656759 \\ 0.142435 & -0.98564 & -0.0906925 & -0.0624323 \\ 0 & 0 & 0 & 1 \end{bmatrix} \tag{3.2}$$

Similarity Transformation Matrix A similarity transformation includes uniform scaling in addition to rotation and translation. The general form is as follows:

$$\mathbf{T}_{\text{similarity}} = \begin{bmatrix} s\mathbf{R} & \mathbf{t} \\ 0 & 1 \end{bmatrix} = \begin{bmatrix} s \cdot r_{11} & s \cdot r_{12} & s \cdot r_{13} & t_1 \\ s \cdot r_{21} & s \cdot r_{22} & s \cdot r_{23} & t_2 \\ s \cdot r_{31} & s \cdot r_{32} & s \cdot r_{33} & t_3 \\ 0 & 0 & 0 & 1 \end{bmatrix} \tag{3.3}$$

where r_{ij} represent the components of the rotation matrix, t_i the translation components and s the uniform scaling factor.

After registration, the similarity transformation matrix obtained from *3DSlicer* with the translation component given in m was:

$$\mathbf{T}_{\text{similarity}} = \begin{bmatrix} 0.786349 & -0.0469391 & -0.00200126 & 0.0147642 \\ 0.0469231 & 0.786331 & -0.00583277 & -0.0134356 \\ 0.0023452 & 0.00570318 & 0.787727 & -0.058686 \\ 0 & 0 & 0 & 1 \end{bmatrix} \tag{3.4}$$

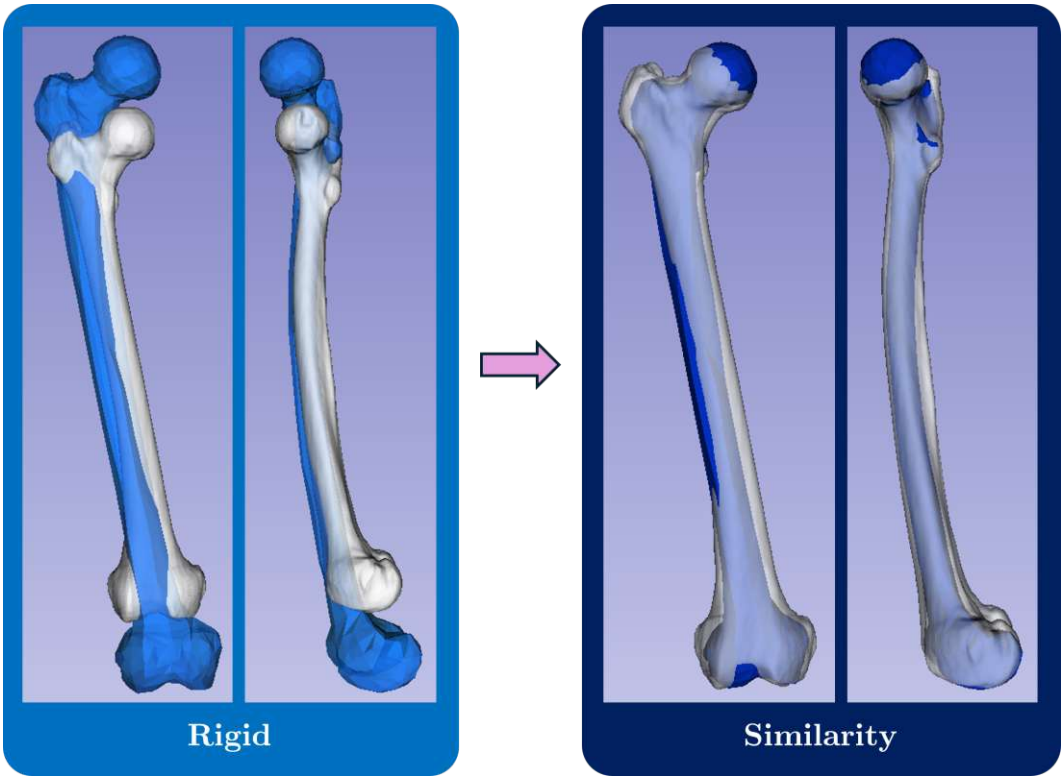

Figure 13: Rigid transformation of the femur geometry of the Gait2392 model (colored) to the patient's femur geometry of the *Hip-Fracture Valid Collection* [2] (white) followed by a similarity transformation.

3.5.3 Image Processing

Image processing of the femoral CT scan of Patient 041 (Section 3.3) was necessary to obtain an ash density-scaled image before generating the FE model. Image processing was conducted in *Medtool*. The CT scan was reconstructed with a anisotropic voxel size of 0.781 25 mm x 0.781 25 mm x 2 mm and 256 × 402 × 230 voxels.

To obtain a mask of the femoral bone, the STL file from the *Hip-Fracture Valid Collection* [2] was used, which represents the triangulated surface geometry of the segmented femur. Using the *GMSH* meshing module [42], the surface mesh was converted into a tetrahedral 3D mesh. An empty image with the same dimensions as the CT scan was created and all voxels inside the tetrahedral mesh were assigned a gray value of 1.

Subsequently, the CT-Scan and the created mask were cropped to a bounding box enclosing the whole femur. Additionally, the originally anisotropic images were resized to an isotropic voxel length of 1 mm x 1 mm x 1 mm, illustrated in Fig. 14 on the left. As a second step the resolution was again modified by coarsing it with a factor of three, setting the voxel side length to 3 mm.

For the material model used later on in this study, each voxel gray value had to be converted from Hounsfield Units (HU) to ash density (ρ_{ash}). This was done by first computing bone mineral density ρ_{CHA} following the relation given in [2], and then computing ρ_{ash} following [57]:

$$\rho_{\text{ash}} = 0.0633 + 0.887 \cdot \rho_{\text{CHA}} \frac{\text{g}}{\text{cm}^3} \tag{3.5}$$

The ash density was then limited to a range of $0 \frac{\text{g}}{\text{cm}^3} < \rho_{\text{ash}} < 1.305 \frac{\text{g}}{\text{cm}^3}$, limits which were derived from raw data of trabecular and cortical bone [57].

Finally, the processed CT scan was masked and an embedding of the bone was applied at the femoral head, shown in Fig. 14 on the right, with a gray value clearly separated from the bone matter. The embedding should facilitate load application to the femoral head in the FE models.

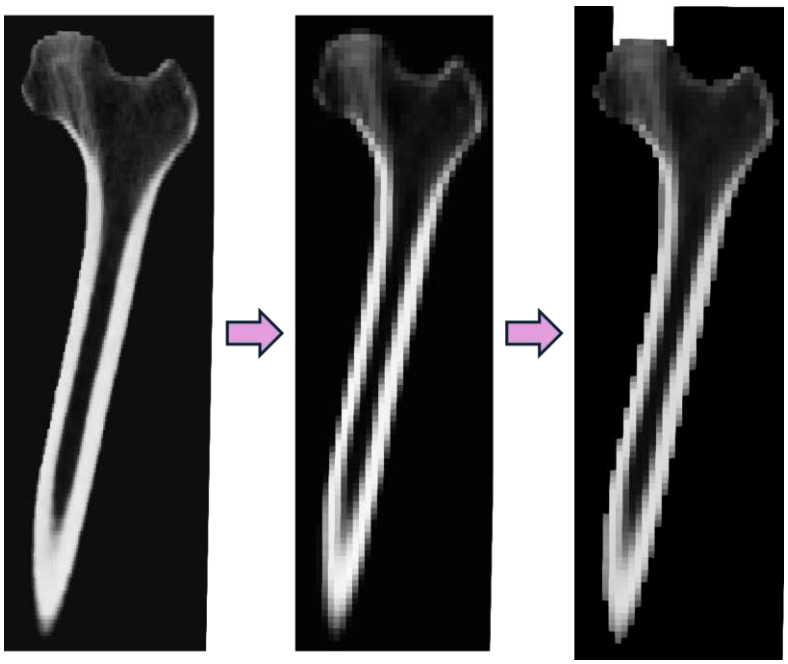

Figure 14: Three stages of the image processing sequence: Femur image with an isotropic side length of 1 mm (left), coarsened isotropic (3 mm), ash density-scaled image (centre) and the masked and embedded femur image (right).

3.5.4 Finite Element Modelling

3.5.4.1 Workflow

The workflow for creating the FE model is illustrated in Fig. 15. First, the fundamental settings for the FE model and simulation were defined via a template file. This included the requested element type, requested node sets, material definitions for bone and embedding, as well as two simulation steps (gait cycle loading and an unloading step) with their respective durations, time increment sizes, and output requests. Additionally, the template included definitions of boundary conditions and load amplitudes that were common to all femoral bones.

The template file and the CT images were then used to generate individual *Abaqus* input decks automatically in *Medtool*, for each of the 93 femora with artificial metastatic lesions. These input files were subsequently further modified with custom scripts to integrate model-specific data required for the application of loads and boundary conditions.

Once all 93 input decks were generated and adapted, FE simulations were carried out in *Abaqus*. To evaluate the failure criterion (see Section 3.7), it was necessary to determine the plastic displacement after unloading. Therefore, if simulations terminated prematurely during the gait cycle, identical reruns were performed with a reduced end time, to ensure the consistent extraction of the plastic displacement despite the premature termination.

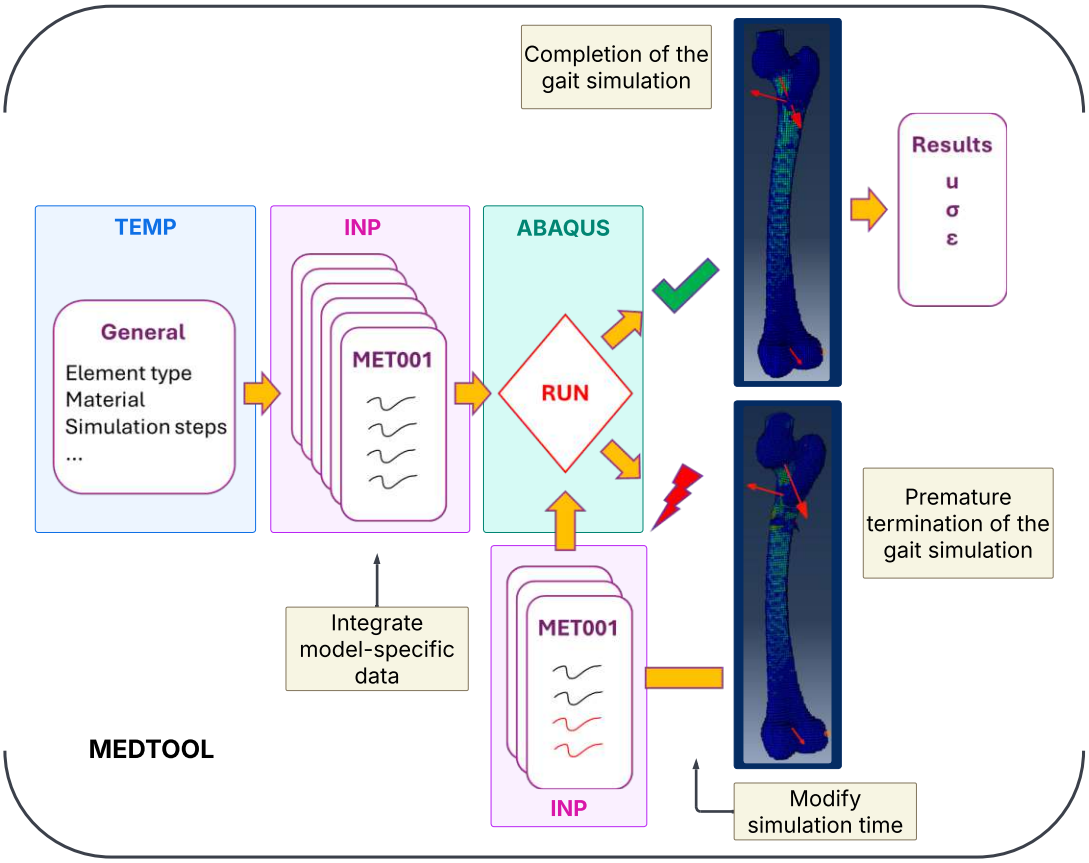

Figure 15: Workflow for the FE model generation: Basic simulation settings and common features across all femora are defined in a template, based on which individual input decks are created. Individual, model-specific data is then added, followed by the execution of the FE simulations with stresses, strains and plastic displacement of the femora as results.

3.5.4.2 Mesh

Each voxel representing bone or embedding was converted to a linear 8-noded fully integrated brick element (C3D8). This resulted in 15585 elements with an element side length of 3 mm.

3.5.4.3 Material

Elements were assigned to element sets based on their ash density. A maximum number of 250 element sets were created, representing ash densities from 0 to $1.305 \frac{g}{cm^3}$. Since the embedding represented homogeneous material with one density, it was assigned a distinct element set. The mesh and resulting element sets of the intact bone are shown in Fig. 16.

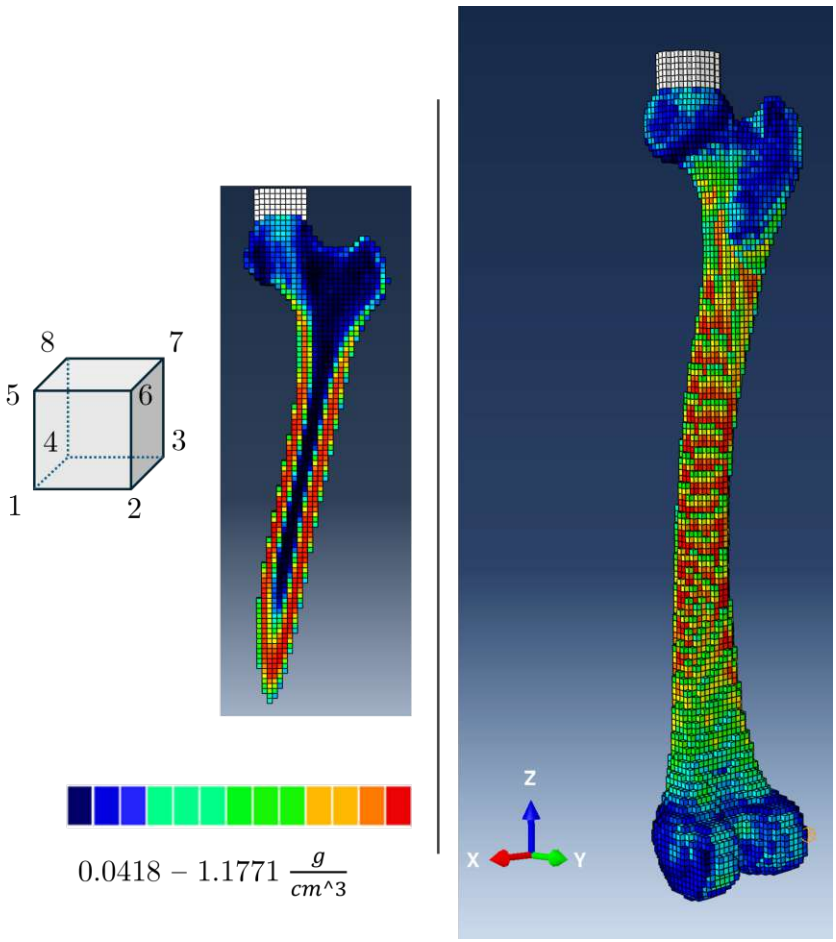

Figure 16: Voxel-based FE mesh of the femur and embedding:
Element sets are colored by corresponding ash density ranging from low density (blue) to high density (red).
Schematic representation of the C3D8-Element (left).

The bone elements of the voxel-based FE mesh were assigned non-linear, isotropic mechanical properties. The material model applied was adopted from Keyak et

al. [57] and is schematically illustrated in Fig. 17. Unless stated otherwise, the following definitions and equations are based on the findings presented in their study.

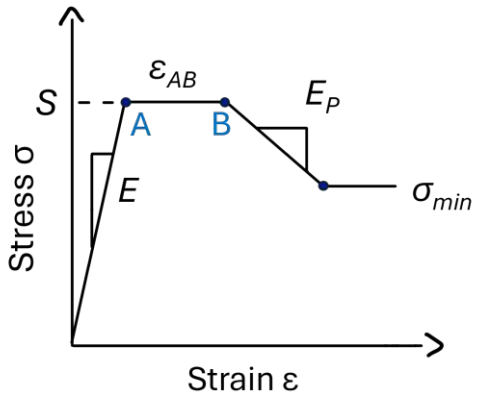

Figure 17: Schematic stress-strain relationship of the applied material model.

The bone material behaviour was defined by an initially elastic response to loading, with a Young's modulus E depending on ρ_{ash}:

$$E = 14900 \cdot {\rho_{\text{ash}}}^{1.86} \text{ MPa} \tag{3.6}$$

After reaching the yield point (A), the material shifted to non-linear behaviour and entered a perfectly plastic phase at yield stress S until a certain strain is reached (ε_{AB}).

$$S = 102 \cdot {\rho_{\text{ash}}}^{1.80} \text{ MPa} \tag{3.7}$$

$$\varepsilon_{\text{AB}} = 0.00189 + 0.0241 \cdot \rho_{\text{ash}} \frac{\text{mm}}{\text{mm}} \tag{3.8}$$

Subsequently, the material entered a linear softening phase with a decreased stiffness expressed by a decreased Young's modulus E_{P}, which is defined as:

$$E_{\text{P}} = -2080 \cdot {\rho_{\text{ash}}}^{1.45} \text{ MPa} \tag{3.9}$$

This softening continued until a minimum stress level σ_{min} was reached:

$$\sigma_{\text{min}} = 43.1 \cdot {\rho_{\text{ash}}}^{1.81} \text{ MPa} \tag{3.10}$$

Beyond this point, the material again exhibited perfectly plastic behaviour.

The relationships presented were derived from both cortical and trabecular bone specimens, except ε_{AB} and E_{P}, which were derived solely from trabecular bone

specimens.
Since the gauge length of the experimental specimens used to determine ε_{AB} and E_P differed from the element side length in the FE model (3 mm), correction terms were introduced for these values.
The corrected expressions for ε_{AB} and E_P are:

$$\varepsilon'_{AB} = \varepsilon_{AB} \cdot \left(\frac{15}{3}\right) \frac{\text{mm}}{\text{mm}} \tag{3.11}$$

$$E'_P = \frac{3 \cdot E \cdot E_P}{15 \cdot E - (15 - 3) \cdot E_P} \text{ MPa} \tag{3.12}$$

To account for the altered mechanical properties in bones affected by metastatic lesions, the relationships between ash density and compressive mechanical parameters were determined using both healthy and metastatic bone tissue [57]. The Poisson's ratio of bone was set to $\nu = 0.3$.

For the embedding material, linear-elastic, isotropic mechanical properties were assigned with a Young's modulus of

$$E_{embed} = 1360 \text{ MPa} \tag{3.13}$$

and a Poisson's ratio of $\nu = 0.3$.

3.5.4.4 Boundary Conditions

The boundary conditions applied to the physiological model were adopted from *Speirs et al.* [92]. To prevent rigid body motion of the femur during the simulation, three anatomical landmarks were defined on its geometry: the hip joint centre, the knee joint centre and the distal lateral epicondyle, as illustrated in Fig. 18.

The knee joint centre was chosen with the aim of locating the midpoint of the intercondylar fossa in both the coronal and sagittal plane. This landmark was fully constrained in all three translational DoF.
The hip joint centre was constrained in two translational DoF, orthogonal to the axis connecting the hip and knee joint centre. This allowed its displacement only along the axis towards the knee joint centre [92]. The position of the hip joint centre was provided along with the CT scan in the *Hip-Fracture Valid Collection* [2] (Section 3.3).
The distal lateral epicondyle landmark was constrained in a single translational DoF orthogonal to the vector from the knee joint centre to the distal lateral epicondyle, as well as orthogonal to the vector from the knee to the hip joint

centre. Thus, this constraint prevented rotation of the femur around the axis between knee and hip joint centre.

To implement these constraints, a local coordinate system was defined. The $\mathbf{x}'$-axis was defined as the vector from the knee to the hip joint centre (Fig. 18). The $\mathbf{y}'$-axis was defined as the vector from the knee centre to the lateral epicondyle. Both $\mathbf{x}'$ and $\mathbf{y}'$ were normalized and the third axis $\mathbf{z}'$ was derived with the cross product:

$$\mathbf{z}' = \mathbf{x}' \times \mathbf{y}' \tag{3.14}$$

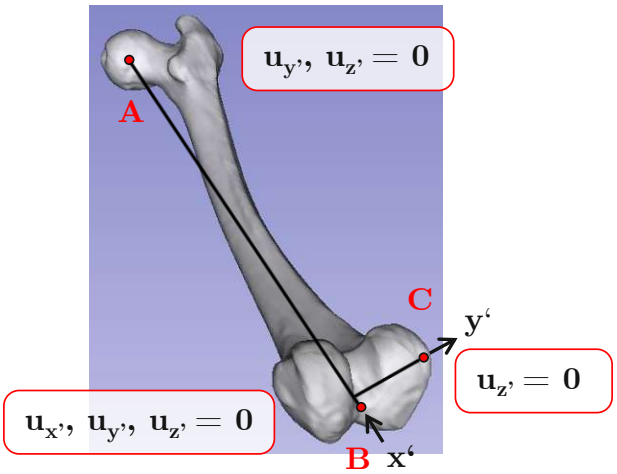

Figure 18: Landmarks and axis to define the boundary conditions: Hip joint centre (A), knee joint centre (B) and distal lateral epicondyle (C).

To prevent unrealistic stresses and thus local failure due to the application of boundary conditions at single nodes, these reference nodes were kinematically coupled to multiple surrounding nodes as described in the following.

Regarding the hip joint centre, a new node was created at the corresponding landmark position and kinematically coupled in all six DoF to the topmost layer of the embedding nodes, which is shown in Fig. 19 on the left. In contrast, no additional nodes were introduced for the distal lateral epicondyle and knee joint centre. Instead, the closest nodes (in terms of euclidean distance) to the respective landmark coordinates were identified and kinematically coupled in all six DoF. Specifically, the distal lateral epicondyle node was coupled to its 24 nearest neighbouring surface nodes, while the knee joint centre node was coupled to its 100 nearest neighbouring surface nodes (Fig. 19 on the right).

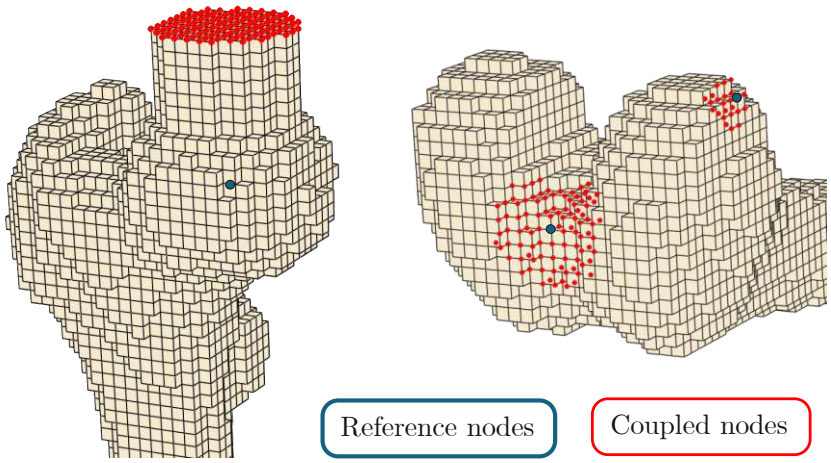

Figure 19: Boundary condition reference nodes and their kinematically coupled nodes in *Abaqus*: Hip joint centre (left), knee joint centre and distal lateral epicondyle (right).

3.5.4.5 Muscle and Hip Joint Force Application

To apply muscle and hip joint forces to the FE model, several steps were necessary. First, the forces and muscle attachment points of the musculoskeletal model were transformed into the FE model's coordinate system. Some muscle attachment points were identified as being spatially very close to each other. As a result, the muscle attachment points of these muscle were merged. Merged attachments were computed as the mean of the respective original points. The following muscle pairs were merged: *Gluteus Minimus 1* and *Gluteus Minimus 2*, *Biceps Femoris - Short Head* and *Adductor Longus*, *Iliacus* and *Psoas Major*, as well as *Gemellus* and *Piriformis*.

The muscle and hip joint force data was reduced to a single gait cycle, beginning and ending with the heel strike of the right foot. The hip joint force was transformed into the local coordinate system via the transformation matrix defined in 3.5.4.4. In cases where muscle attachments had been merged, both muscles were separately defined to act on one shared muscle attachment point.

Muscle forces were all introduced as concentrated forces at their attachment points and and the hip joint force was applied at the hip joint centre. For the hip joint centre, which was already kinematically coupled as part of the boundary condition implementation, nothing more had to be done.
To apply the muscle forces, a reference node was defined as the surface node with the lowest euclidean distance to the muscle attachment point from the

musculoskeletal model. To avoid unrealistic stress concentrations here as well, each muscle node was kinematically coupled in all six DoF to surrounding mesh nodes. In most cases, a coupling with the 24 nearest neighbouring nodes was sufficient to avoid excessive stresses. However, in case of very high magnitudes of exerted muscle force, additional nodes were added to better distribute the force. Specifically, for the *Gastrocnemicus Medialis* and the merged *Ilio-Psoas* muscle, coupling was extended to include additional 100 nearest neighbouring surface nodes.

3.6 Simplified Model

In contrast to the physiological model, the workflow for the simplified model was considerably reduced, focusing solely on the application of the peak hip joint force. The corresponding workflow is visualized in Fig. 20.

From the complete gait cycle simulation conducted in *OpenSim*, only the peak hip joint force was extracted. In order to apply this force to the patient-specific femur geometry, it was transformed using the same registration procedure as described in 3.5.2. Separately, the CT scan was processed with *Medtool* following similar steps as for the physiological model.

The mesh and material information derived from the CT scan, along with the customized peak hip joint force from *OpenSim*, was then implemented into *Abaqus* for the FE simulation.

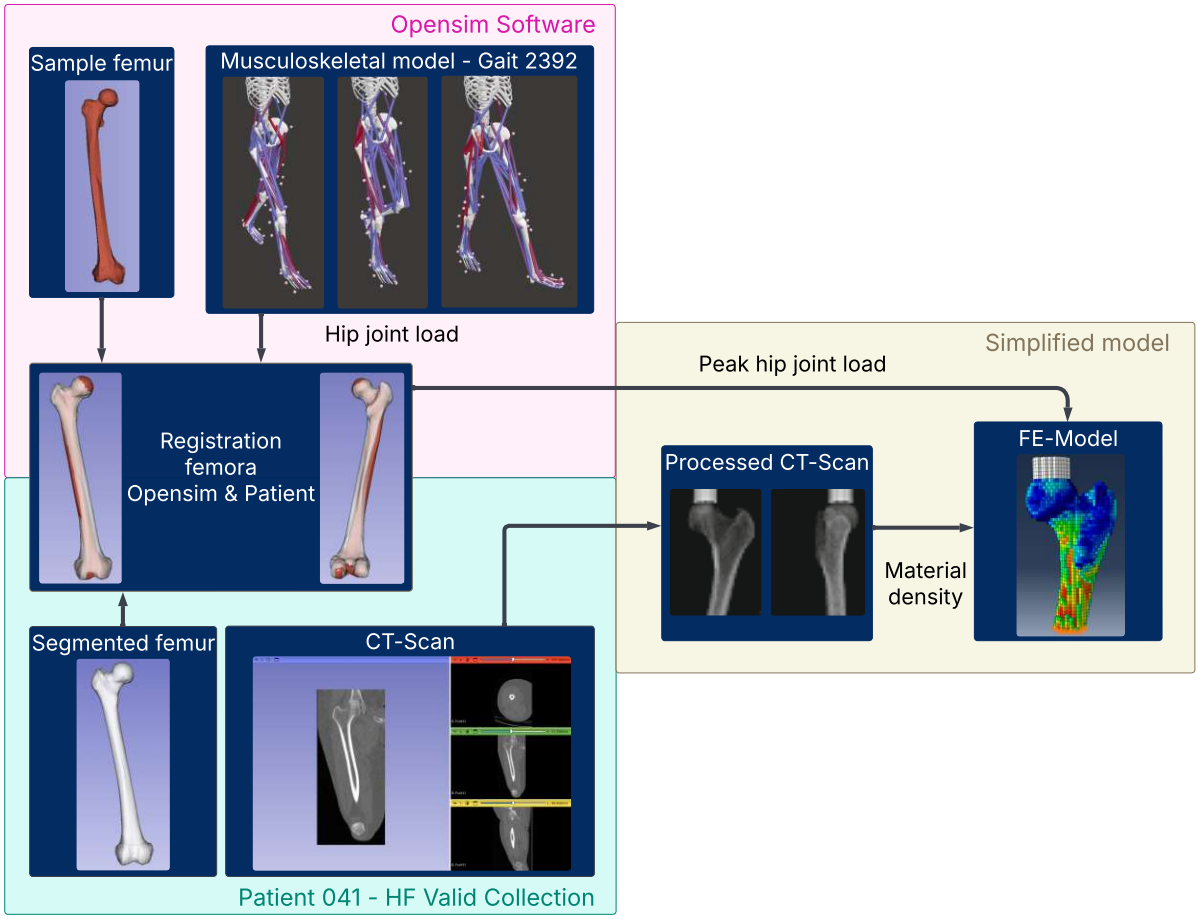

Figure 20: Workflow for the simplified model.

3.6.1 Image Processing

The image processing of the CT scan for the simplified model was largely identical to the one described for the physiological model (Section 3.5.3).

However, a key difference was that prior to coarsening the resolution by a factor of three, both the image and the corresponding segmentation mask were cropped to approximately 36% of its original length. This step aimed to reduce computational effort while preserving predictive performance and was determined in a convergence study (see Section 3.6.2.3).

3.6.2 Finite Element Modelling

The process of constructing the FE model using the simplified approach was largely identical to that of the physiological approach. The workflow, meshing and material properties were established and implemented in the same manner as described in Section 3.5.4. Therefore, these aspects will not be reiterated again. The resulting model with an element number of 6174 and with element sets colored by respective ash density values is shown in Fig. 21.

3.6.2.1 Boundary Conditions

The boundary conditions applied in the simplified model differed from those used in the physiological model. All nodes located at the distal end of the cropped bone were simply fully constrained, thereby restricting each node in the plane in all 3 translational DoF.

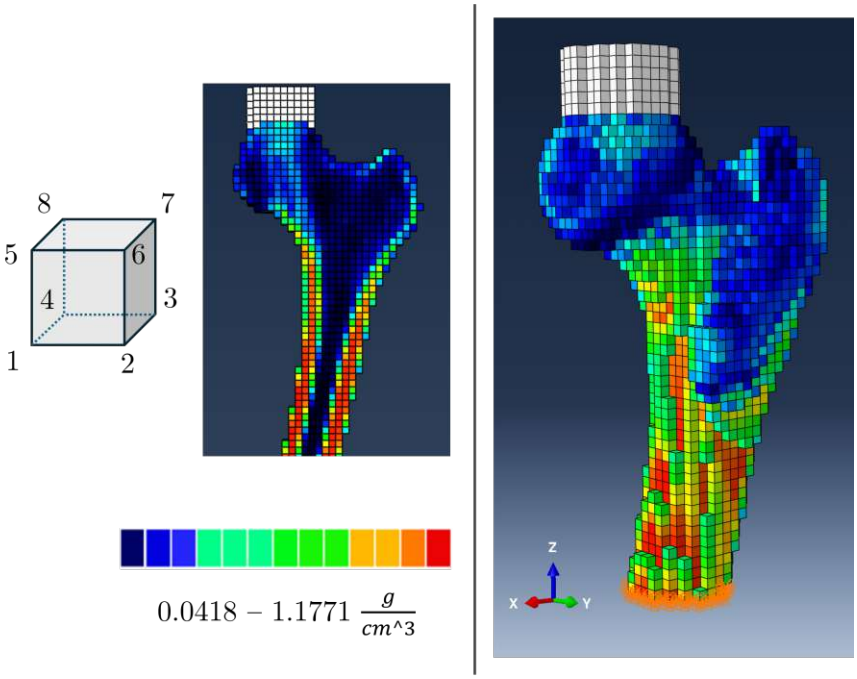

Figure 21: Voxel-based FE mesh of the femur and embedding:
Element sets are colored by corresponding ash density ranging from low density (blue) to high density (red).
Schematic representation of the C3D8-Element (left).

3.6.2.2 Hip Joint Force Application

As with the physiological model, a coordinate system transformation was performed to convert the hip joint centre position into the FE model coordinate system. Subsequently, the peak hip joint force was extracted from the complete gait cycle simulation. In order to apply the force at the hip joint centre, a node was created at the transformed position and kinematically coupled in all six DoF to the topmost layer of the embedding nodes. The peak hip joint force was then introduced as a concentrated force, with the help of a local coordinate system defined along its direction. The application of the force followed a linearly ramped profile, in which the force magnitude increased gradually till its target value.

3.6.2.3 Investigation of Bone Length

Initially, the femur was cropped at 50% of its original length. However, in combination with fully constraining the bone at its distal end and the application of the oblique hip joint force vector at the hip joint, excessive plastic strain developed at the distal end of the bone.

To determine the bone length at which failure becomes independent from bone length, the femur was progressively shortened. The objective was to determine the bone length range at which the fracture site varied from the clamp and predicted ultimate forces reached a plausible value range. Nevertheless, care was taken to preserve as much bone length as possible, since excessive cropping would limit the capacity to simulate metastases in different anatomical regions. For this purpose, a series of FE models was created, each subjected to displacement-driven loading in direction of the peak hip joint force, applied at the hip joint centre. Force–displacement curves were recorded for each bone length, called sections in the following. Section 0 corresponds to the bone cut at 50% of its length, while section 9 represents the shortest bone configuration, cut at 25%. The bone sections, along with their corresponding ultimate forces are shown in Fig. 22.

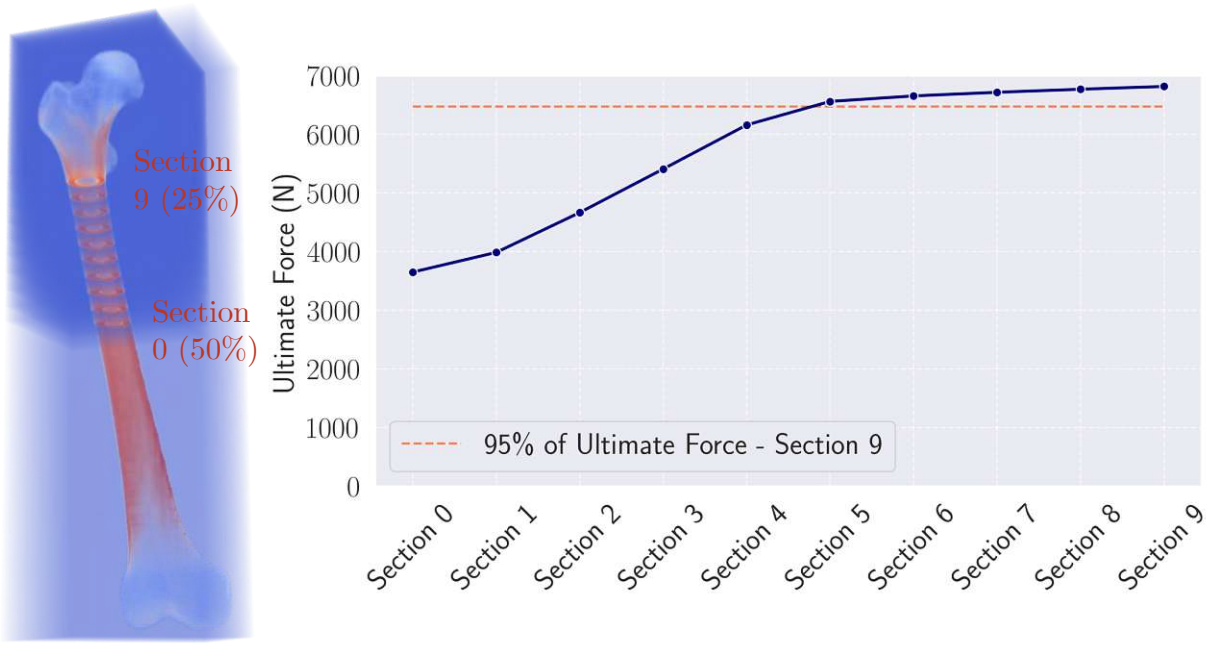

Figure 22: Ultimate forces for progressively shortened bone sections, with the bone sections shown on the left.

The first bone length that fulfilled both criteria, fracture no longer occurring at the clamp and an ultimate force within 95% of that recorded for the shortest section, was section 5. To preserve as much bone length as possible, this section was chosen for the further simulation.

3.7 Failure Criterion for the Finite Element Models

To classify the bones into either "fractured" or "non-fractured" after application of (physiological) loading, a failure criterion had to be defined. Defining such a criterion based on FE models is challenging, particularly since they often include only elastic or elasto-plastic material behaviour (Section 1.2.2). In this study, a bone is considered as "fractured" if irreversible deformation of the hip joint centre beyond a given threshold is observed after just one loading cycle. The threshold value selected in this case was 0.1 mm. This criterion is considered more robust than declaring the bone as "fractured" after a certain number of elements exceed

stress or strain thresholds (e.g. see [58, 94]), and has the advantage that it can be physically interpreted.

To evaluate this failure criterion, the simulation was conducted in two steps: a loading and a relief step. In the first simulation step, the relevant load(s) were applied as described in Sections 3.5.4.5 and 3.6.2.2. In the second step, all previously applied loads were gradually removed using a linearly ramped profile, mirroring the manner in which they were applied. The plastic displacement of the hip joint centre was extracted from all simulations that completed the load–relief cycle. For simulations that terminated prematurely, identical reruns were performed with a reduced end time, allowing consistent extraction of the plastic displacement despite the premature termination.

3.8 Sample Selection

In total, 914 femora with artificially inserted lesions were available for this study. However, since lesion placement was random, the distribution between the "fractured" and "non-fractured" group was potentially imbalanced. To ensure a balanced study sample, the bones were classified into three subgroups: safe, borderline, and critical. In addition, this approach allowed for insights into the models' performance across these different categories.

To classify the bones, an additional FE model was created, closely resembling the simplified model in this thesis, but implemented as displacement-driven model instead of a load-driven one. That means instead of a concentrated force, a displacement of 5 mm was prescribed at the hip joint centre in direction of the peak hip joint load. Apart from this modification, all other aspects were adopted from the simplified model. After conducting these simulations, force-displacement graphs of the hip joint centre in displacement direction were recorded and the ultimate force of the bones with metastases determined.

The peak hip joint load of one gait cycle of 3006.48 N determined in the musculoskeletal models then served as a reference for defining the subgroup limits. Bones with an ultimate force within a range of ±900 N around the peak hip joint load were classified as borderline cases. Bones with an ultimate force above were classified as safe cases, while bones with an ultimate force below formed the critical subgroup.

With the creation of the three subgroups, an equal number of specimens could be selected from each subgroup. In this study, 31 bones with artificial metastases were randomly chosen from each subgroup, resulting in a total sample of 93 metastatic

cases. The sample distribution is illustrated in Fig. 23, where each point represents a metastatic case. The peak hip joint load and the three subgroups evolving around it can be seen as well.

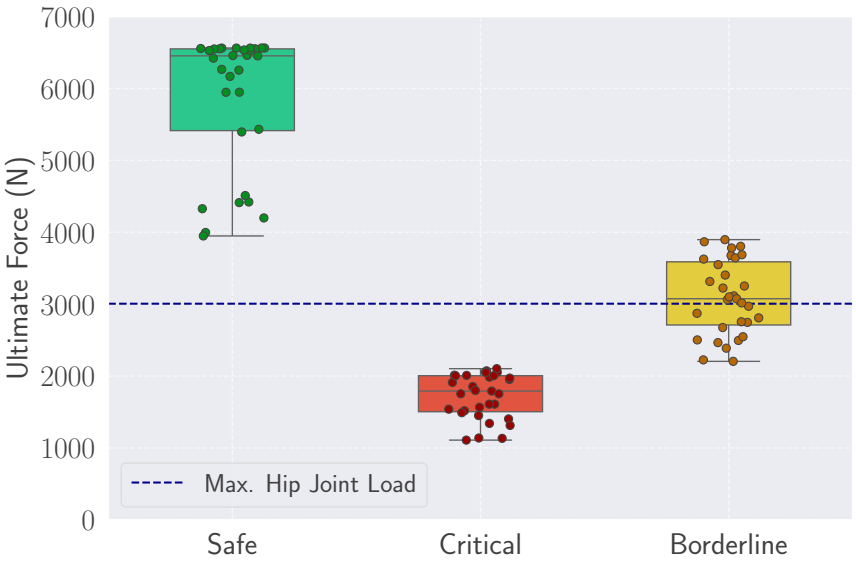

Figure 23: Subdivision of the sample in three subgroups around the peak hip joint load: safe (green), borderline (yellow) and critical (red).

3.9 Metrics for comparison

The two FE modelling approaches, physiological and simplified, differed substantially in terms of model complexity, computational effort and data input requirements. To assess their respective predictive capabilities, a structured comparison was conducted.

Firstly, the mechanical response of the intact femur was investigated. For the physiological model, muscle and hip joint forces throughout the gait cycle were examined and related to the resulting stress distribution and deformation. For the simplified model, the stress distribution and deformation was examined in response to the peak hip joint force.

Subsequently, femora with artificially inserted metastatic lesions were analysed. Representative cases were selected to highlight similarities and differences in stress distribution and plastic strains between the two approaches.

The failure criterion of Section 3.7 was then used to classify each of the 93 femora with metastatic lesions as "fractured" or "non-fractured" with both FE modelling approaches. The agreement of the model predictions could then be evaluated using a confusion matrix. In addition, the agreement was evaluated for each subgroup (safe, borderline, critical).

Finally, the impact of the metastasis location was investigated: first, by investigating the location of metastases that led to prediction discrepancies, and second by an evaluation of prediction agreement across anatomical femur regions.

To illustrate the prediction agreement across anatomical femur regions, the centres of all metastases were marked in an anterior-posterior projection of the femoral bone. The bone was then subdivided into anatomically defined regions (femoral neck, femoral head, greater trochanter, intertrochanteric region and proximal femoral shaft), illustrated in Fig. 24. The placement and dimension of each Region of Interest (RoI) was loosely based on a Dual-energy X-ray Absorptiometry (DXA) study by *Slart et al.* [91], intended to support interpretability. The prediction agreement between the physiological and simplified model was subsequently computed for each region separately.

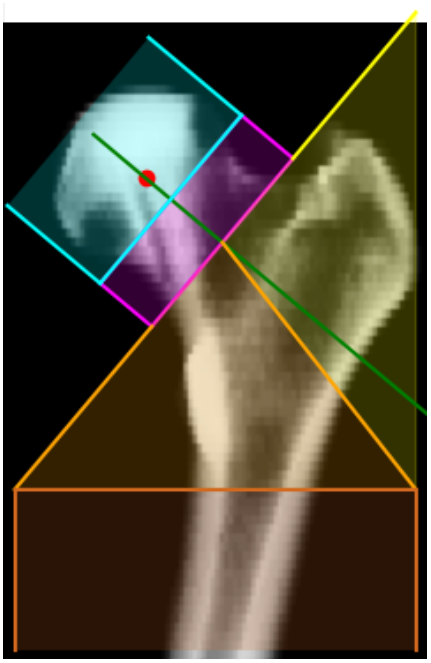

Figure 24: Femoral projection with the anatomical regions of interest: head (blue), neck (pink), greater trochanter (yellow), intertrochanteric region (orange) and proximal shaft (brown).

Region boundaries were defined geometrically: the femoral neck RoI (width: 1.5 cm, length: 1.5 cm) was placed at an angle of 40° relative to the vertical axis. An auxiliary line orthogonal to its long side served to define the boundary line between greater trochanter and intertrochanteric RoI (angle: 12°). The border between intertrochanteric and proximal shaft RoI lay approximately 0.5 cm distal the lesser trochanter.

4 Results

The following chapter presents the results of the conducted simulations. Initially, the investigation focuses on the intact femur, illustrating occurring muscle and hip joint forces throughout the gait cycle, along with the corresponding stress distribution within the bone and observed plastic strains. In this process, the physiological and simplified FE model are compared.

Subsequently, the focus is directed towards the 93 femora with artificial metastatic lesions. As described in 3.9, selected example cases are examined to qualitatively assess differences in deformation, stress and plastic strain distribution between the the physiological and simplified FE model. Furthermore, the overall agreement of fracture predictions between the modelling approaches is evaluated across all sample bones.

4.1 Model Comparison in the Intact Femur

4.1.1 Muscle and Hip Joint Forces

The forces of all muscles acting on the femoral bone, along with their corresponding activation are shown in Fig. 25. Muscle forces are indicated in blue, while muscle activations are indicated in red. The plots depict one full gait cycle, beginning and ending with the heel strike of the right foot.

As it can be seen, the *Gastrocnemicus Medialis* exerted the highest among all muscles reaching a maximum of approximately 1500 N at full activation at 44 % of the gait cycle. Besides, the *Iliacus*, *Psoas Major* and *Gluteus Medius* were major contributing muscles with the first two reaching a force of approximately 750 N at around 85 % activation at 53 % of the gait cycle. The *Gluteus Medius* peaked simultaneously with the *Gastrocnemicus Medialis* at approximately 50 % activation resulting in a force close to 900 N.

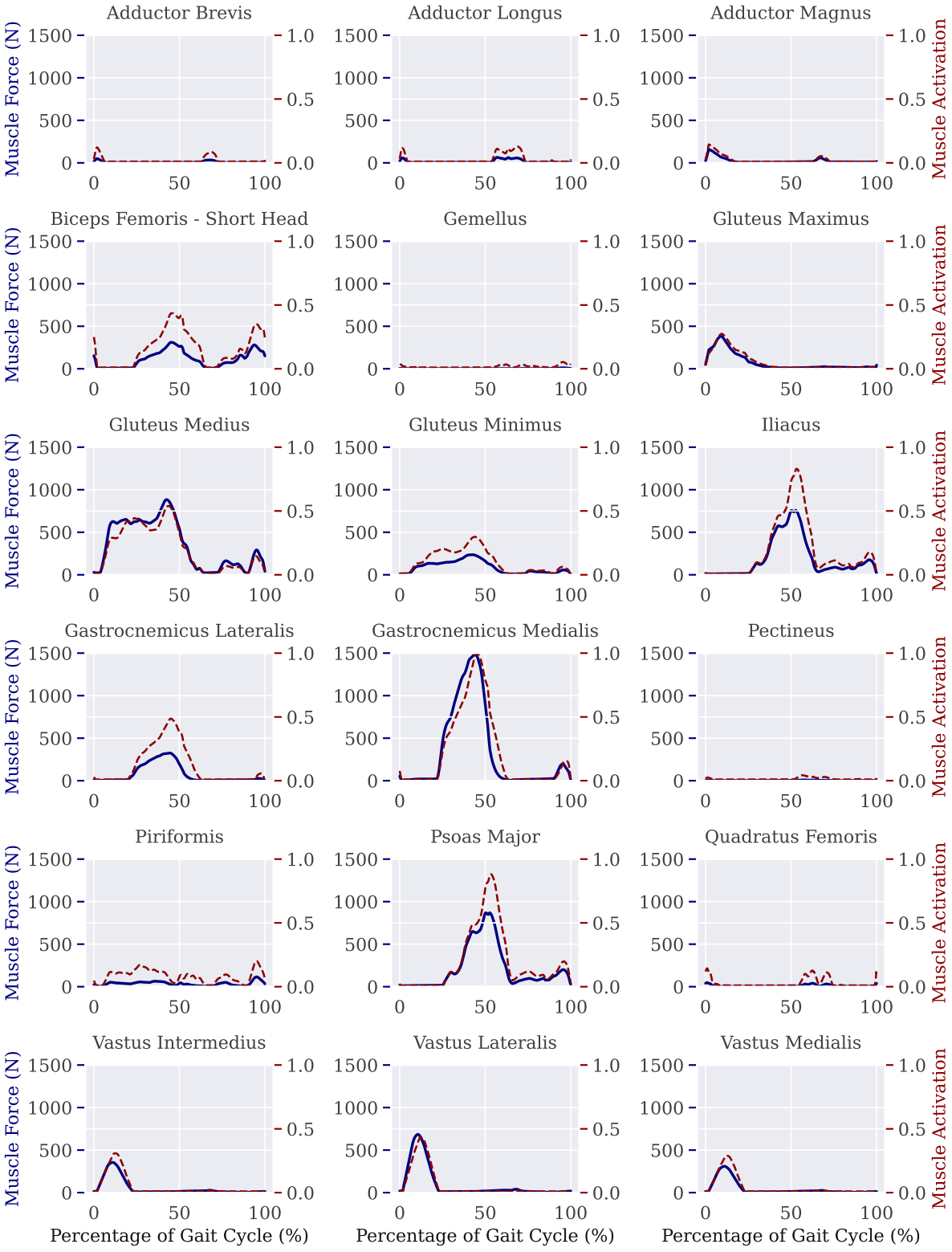

Figure 25: Resulting muscle forces and muscle activations during the gait cycle.

However, the greatest load acting on the femur was the hip joint force as illustrated at the top of Fig. 26. The maximum joint force occurred at 43 % of the gait cycle, reaching 3006 N (indicated by the second red line (2) in Fig. 26). Another characteristic time point corresponded to the peak forces of the *Iliacus* and *Psoas Major* muscles, indicated by the third red line (3), which were accompanied by a hip joint force of 2590 N. A further, albeit smaller, peak in hip joint force occurred at 10 % of the gait cycle ((1) in Fig. 26) with a force of 2250 N.

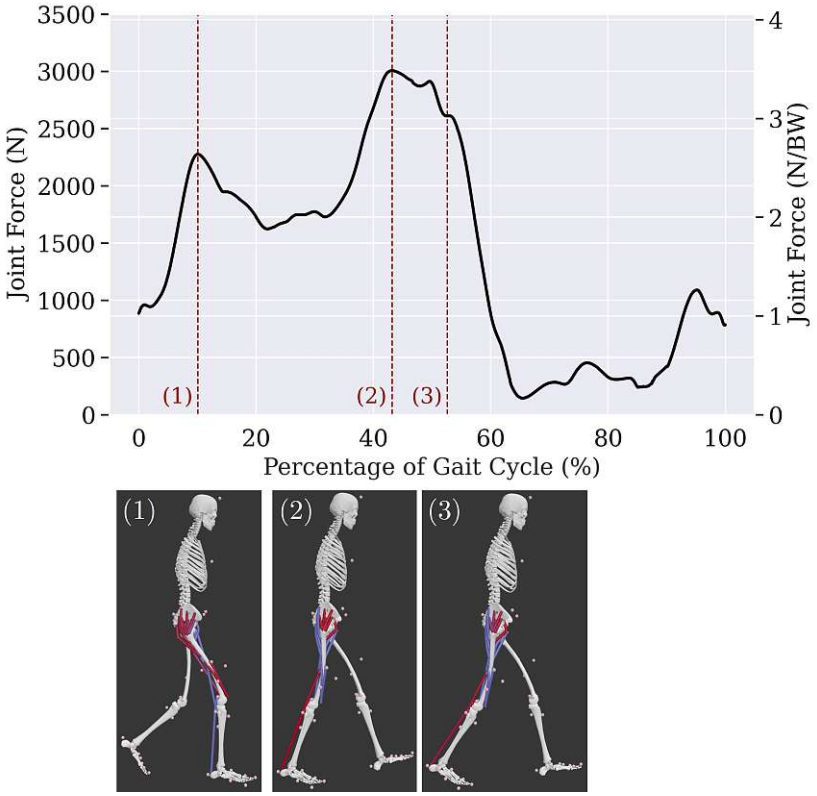

Figure 26: Hip joint force during the gait cycle in three characteristic load situations ((1), (2), (3)) and the associated movements.

An examination of the specific movements at these time points emphasized the importance of single-leg stance transitions regarding hip joint force, more precisely the loading response to and push-off from the one-legged stance. The specific movements are illustrated in Fig. 26 on the bottom.

The first and smallest of the three peaks identified, occurred at the left foot toe-off, initiating a weight shift to the right leg. At this stage, muscles at the greater trochanter as well as the *Vastus* muscles (lateralis, medialis, intermedius) got activated in addition to the hip joint force, depicted in Fig. 27a.

The peak hip joint force was observed during the terminal stance phase of the right leg, shortly before the heel strike of the left foot. Next to the hip joint force, the *Gastrocnemicus Medialis* and the *Gluteus Medius* exerted their peak force. Furthermore, the combined *Ilio-Psoas* muscles contributed significantly to the loading condition, depicted in Fig. 27b.
The last peak investigated occurred shortly after, during the pre-swing phase, when the right foot pushed off to shift weight to the left leg. As previously mentioned, the *Ilio-Psoas* muscles exerted their peak force, which is shown in Fig. 27c.

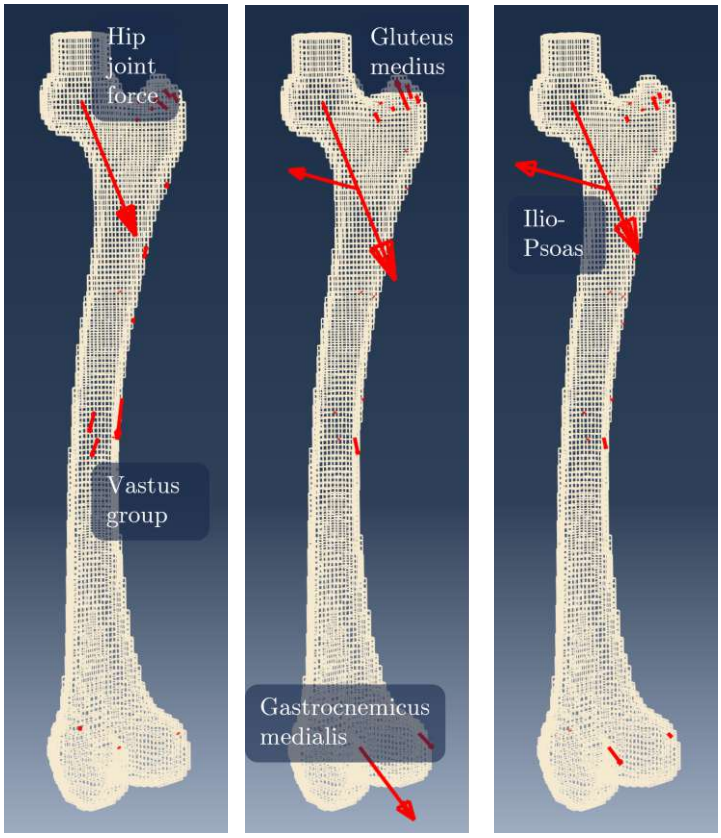

(a) 10 % of GC (b) 43 % of GC (c) 53 % of GC

Figure 27: Muscle and hip joint forces at three distinct time points during the Gait Cycle (GC), with the most prominent muscles labelled.

The figures presented correspond to the physiological modelling approach with individual muscle forces, whilst the simplified modelling approach only considered the peak hip joint force shown in Fig. 26 (2) and 27 (b).

4.1.2 Deformation and Stress Results

The investigation of stress and global deformation in the intact femur is structured in accordance with section 4.1.1, focusing on three characteristic stages (10% GC, 43% GC, and 53% GC) of muscle and hip joint loading during the gait cycle in case of the physiological model. In case of the simplified model the analysis reduces to the moment of peak hip loading.
Stresses are reported and visualized as the von Mises equivalent stress, if not stated differently. To enhance the visibility of the deformation patterns, a uniform deformation scale factor of 6 was applied for all visualizations in this section except the sectioned views.

The displacement of the femur is visualized in Fig. 28 and 29.

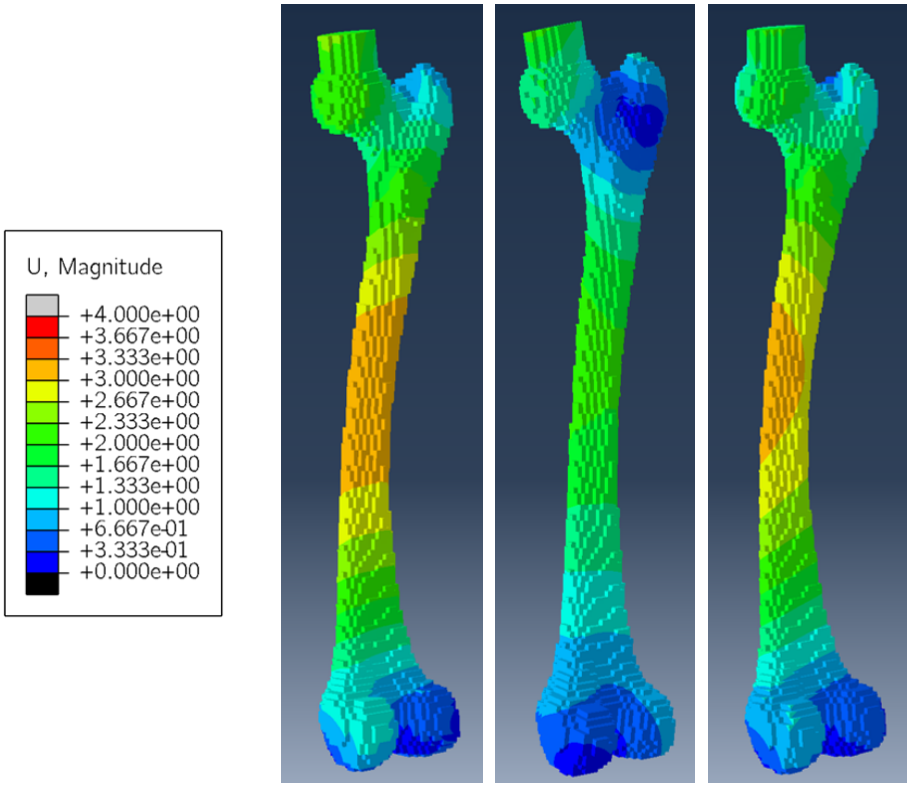

(a) 10 % of GC (b) 43 % of GC (c) 53 % of GC

Figure 28: Physiological Model: Displacement of the femur at three distinct time points (deformation scale factor of 6).

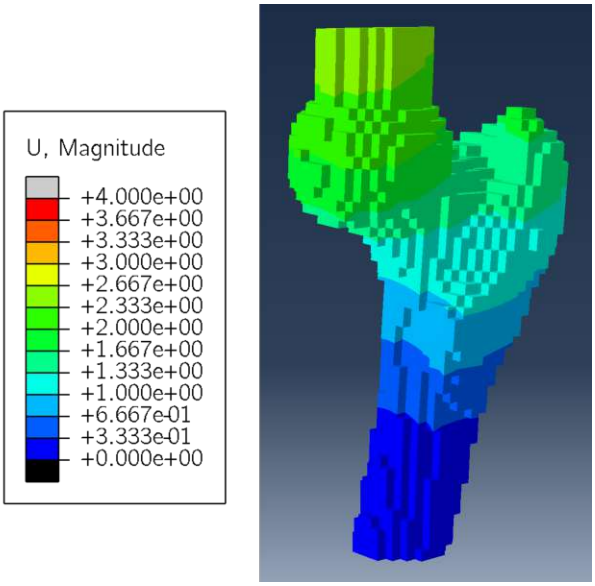

Figure 29: Simplified Model: Displacement of the femur at the moment of peak hip joint loading (deformation scale factor of 6).

As shown in Fig. 30a and 31 for the physiological model, the loading scenario with the hip joint force as the prevalent force and comparatively minor muscle contributions (10 % GC), led to stresses in the proximal shaft at the lesser trochanter, as well as in the distal shaft region. Bending of the proximal femur, particularly the femoral head, was observed in the coronal plane in inferior direction, whereas bending of the femoral shaft was observed in the sagittal plane in anterior direction.
At the moment of peak hip joint loading (43 % GC), bending in the sagittal plane decreased, partly due to a strong *Gastrocnemicus Medialis* force, while it remained unchanged in the coronal plane. A shift in stress distribution was observed, as it decreased in the femoral shaft and increased slightly at the lesser trochanter and in the femoral neck.
In the subsequent loading scenario (53 % GC), bending in the sagittal plane increased once more, reaching its greatest extent. Simultaneously, stress increased in the femoral neck and the proximal femoral shaft.

A comparison with the simplified model, shown in Fig. 32 and 31, revealed only small differences. Seemingly smaller bending of the femoral head was observed in the coronal plane in inferior direction, while posterior bending of the femoral head and greater trochanter occurred in the sagittal plane, identical to the physiological model.
Stresses were observed in the femoral neck and proximal shaft at the distal fixation.

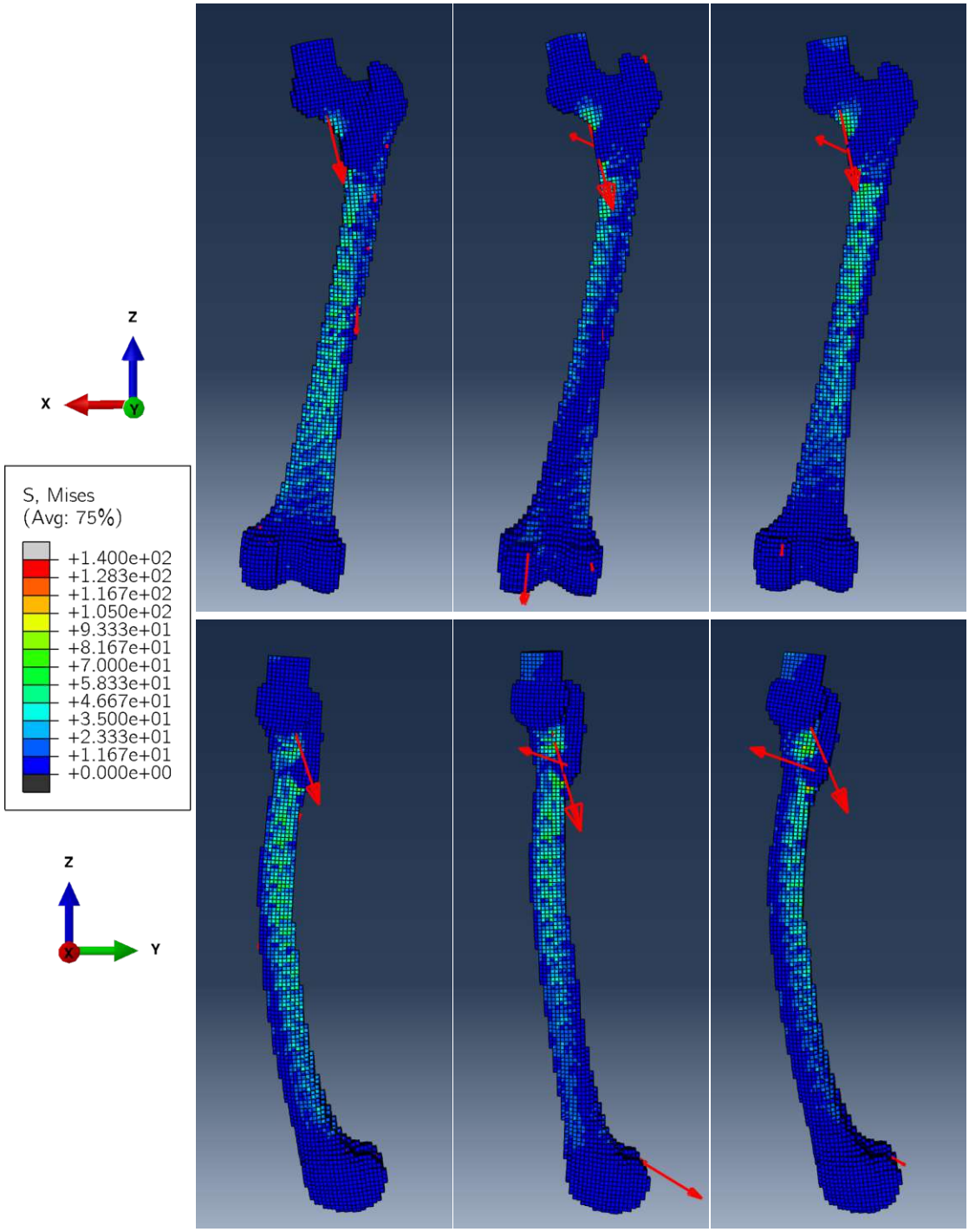

(a) 10 % of GC (b) 43 % of GC (c) 53 % of GC

Figure 30: Physiological Model: Stress distribution at three time points in posterior- and medial view, with a deformation scale factor of 6.

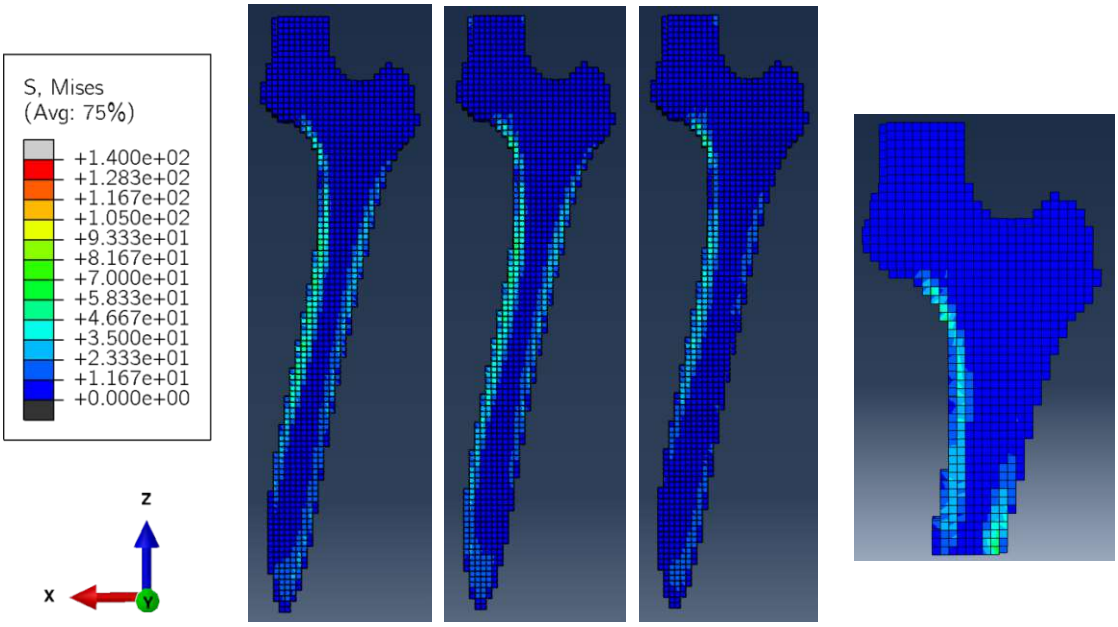

(a) 10 % of GC (b) 43 % of GC (c) 53 % of GC

Figure 31: Physiological and Simplified Model: Internal stress distribution with suppressed bone deformation and an equal cutting plane.

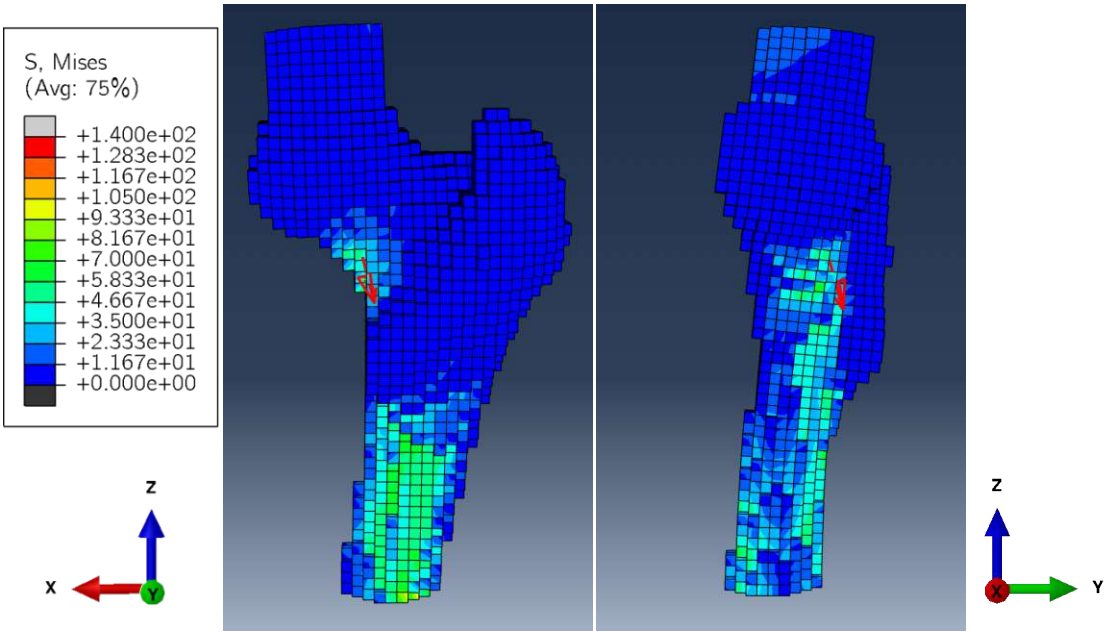

Figure 32: Simplified Model: Stress distribution at the moment of peak hip joint loading (43 % of GC) in posterior- and medial view, with a deformation scale factor of 6.

Following the evaluation of stress distribution and global deformation, the occurrence of plastic strain in the bone was investigated. This was quantified by the equivalent plastic strain $PEEQ$.

Minor plastic strain occurred within two time intervals of the gait cycle. The first interval, from 31 % to 43 % of the gait cycle, coincided with the peak activation of the *Gastrocnemicus Medialis*. Plastic strain was localized at the posterior superior part of the medial femoral condyle, near the *Gastrocnemicus Medialis* attachment site. The second interval spanned from 47 % to 53 % of the gait cycle with minor plastic strain localized proximal of the lesser trochanter at the *Ilio-Psoas* insertion, as well as in the femoral neck.

In contrast to the physiological model, no local plastic strain was observed in case of the simplified model.

4.2 Model Comparison in Femora with Metastatic Lesions

4.2.1 Deformation, Stresses and Failure Locations

The investigation of stress, plastic strain and if applicable, failure locations, for metastatic femora is structured differently than the preceding sections. Given the large number of femora with metastatic lesions, only a few representative femora are presented in detail.

Stresses are reported and visualized as von Mises equivalent stresses and deformation scale factors of six were used in visualizations if not denoted differently. If a simulation was prematurely terminated in *Abaqus* and failed according to the fracture criterion, the moment immediately prior to termination is investigated for stress analysis and the state after load and relief for the plastic strain analysis. In simulations that were not prematurely terminated, the moment exhibiting the highest stress is investigated for stress analysis.

Figure 33 shows the simplified model femora of the three following examples, with the metastatic lesions marked by a notably reduced bone mineral density.

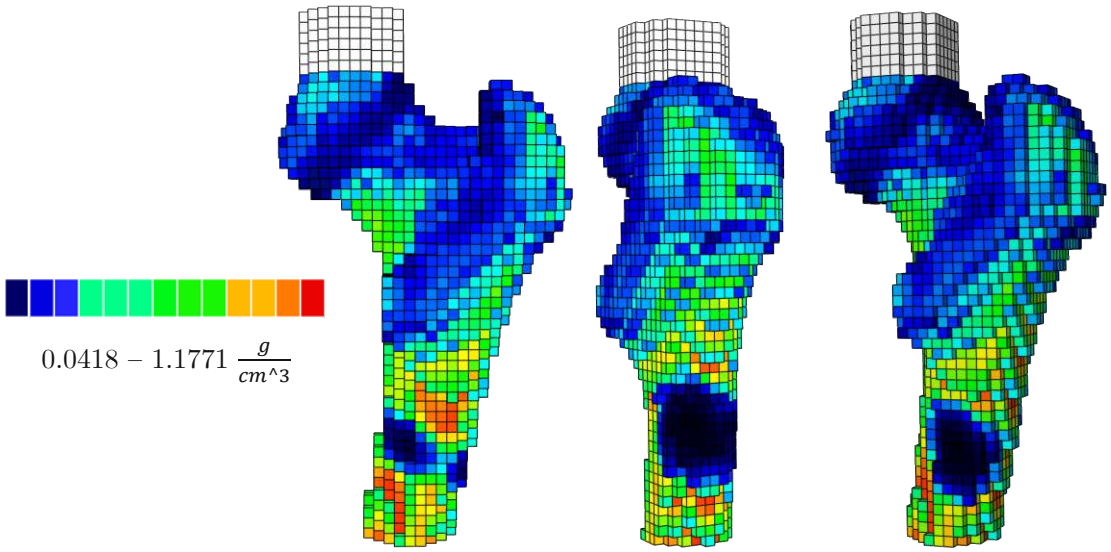

Figure 33: Simplified model femora 615 (left), 319 (centre) and 571 (right) with the metastatic lesion marked by a reduced bone mineral density.

In case of a matching fracture prediction between the FE models, the majority of cases exhibited similar stress distributions and matching patterns of plastic strains. This then led subsequently to bone failure in a similar way for the predicted fracture cases. Such an example is depicted in Fig. 34.
As illustrated in Fig. 34, stress around the metastasis and fracture location was largely consistent for both models. In both models, large plastic strains were observed at the lesion location. Additionally, minor plastic strains were visible in the physiological model, as already described in Section 4.1.2.

Nevertheless, a notable number of cases showed differences in either stress distribution or plastic deformation patterns, despite both models classifying the bones as fractured. An example of such is pictured in Fig. 35.
In this example, the stress distribution was consistent, with local maxima located around the metastasis location. However, plastic strains differed: large plastic strains were observed in the medial shaft region in the the physiological model, whereas the simplified showed plastic strains predominantly in the posterior shaft region.

In cases of contradicting fracture predictions between the models, as illustrated in Fig. 36, stress and plastic strain were mostly located in the same areas within the bone, although their extent varied considerably between the models.

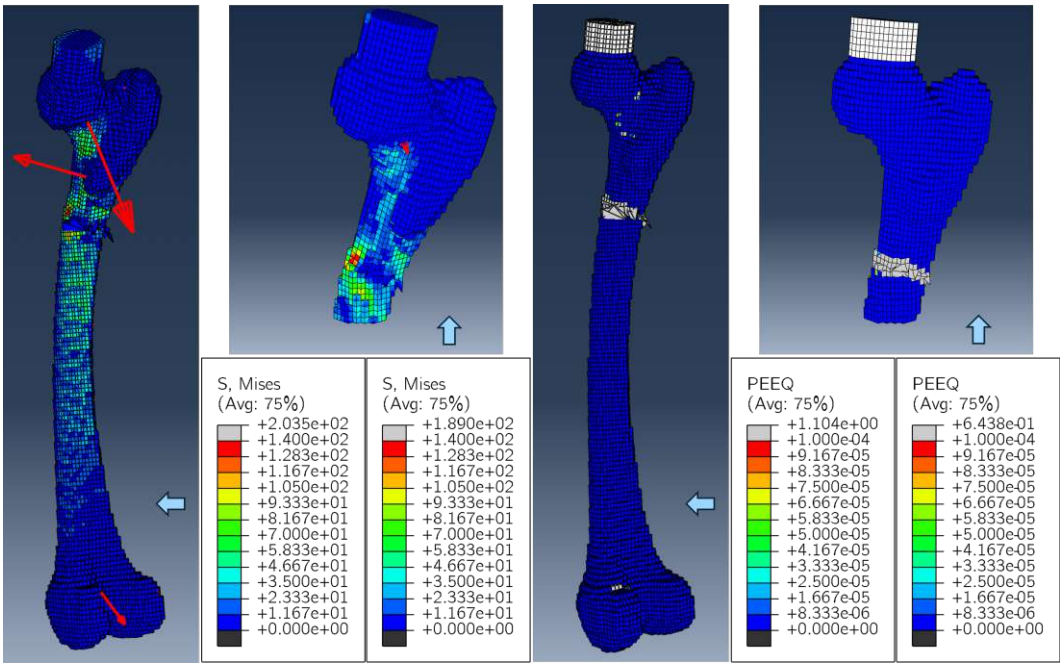

Figure 34: Stress and plastic strain within metastatic femur 615 (deformation scale factor of 6). Both models classified the femur as fractured.

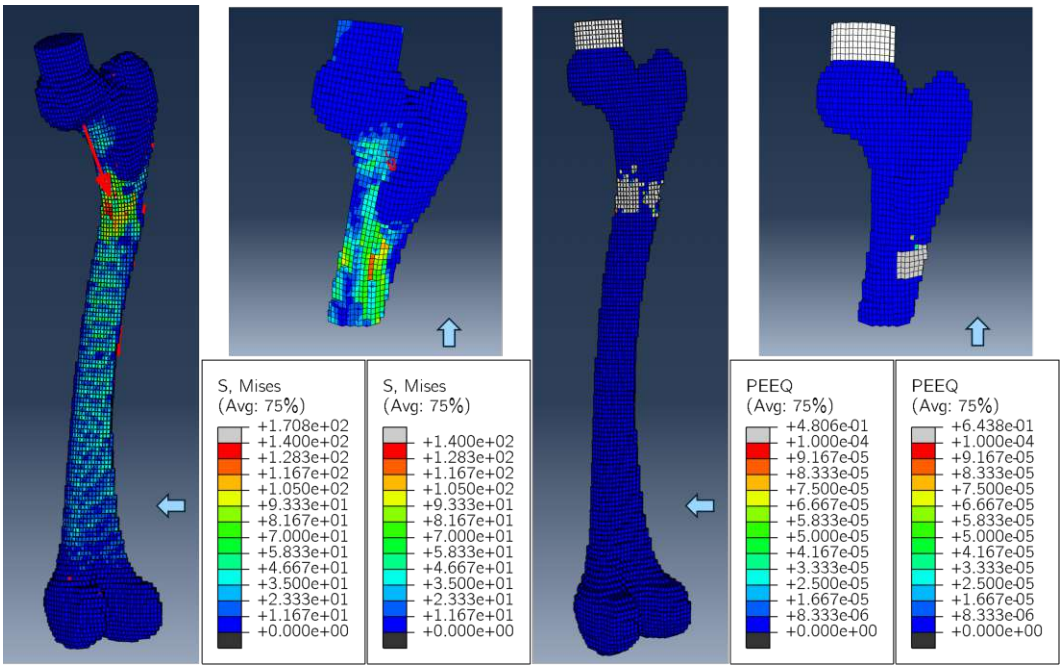

Figure 35: Stress and plastic strain within metastatic femur 319 (deformation scale factor of 6). Both models classified the femur as fractured.

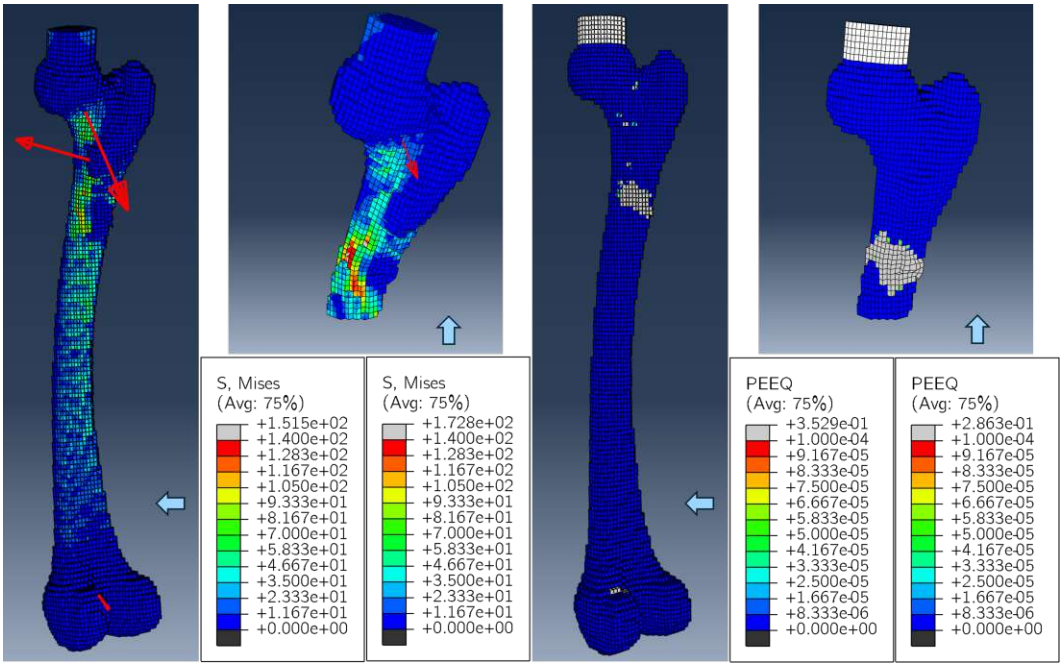

Figure 36: Stress and plastic strain in metastatic femur 571 (deformation scale factor of 6). The simplified model classified the femur as fractured, in contrast to the physiological model.

4.2.2 Agreement of Fracture Predictions

The overall results of the fracture predictions obtained with both models across the entire sample are displayed in Fig. 37.

54 out of 93 bones with artificial metastatic lesions were classified as fractured with both modelling approaches, 30 out of 93 were classified as non-fractured. 6 cases were classified as fractured by the simplified model, while the physiological model classified them as non-fractured. On the contrary, 3 cases were classified as fractured by the physiological model and non-fractured by the simplified model. In total, this resulted in an accuracy of 90.32 % in terms of the prediction agreement between the models.

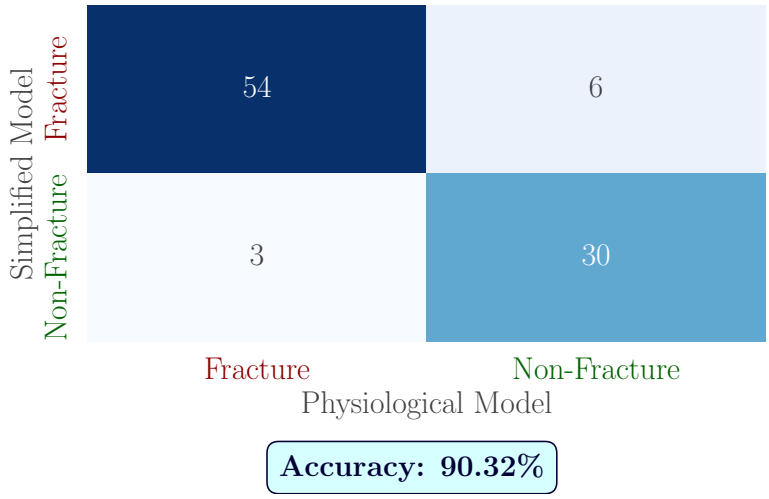

Figure 37: Confusion matrix of the fracture predictions across the entire sample.

The subdivision of the sample into "safe", "borderline", and "critical" cases, as introduced in Section 3.8, allowed for a more detailed evaluation of the results. As shown in Fig. 38, accuracies of 90.32 %, of 80.65 % and of 100 % were achieved for the "safe", "borderline", and "critical" subgroups.

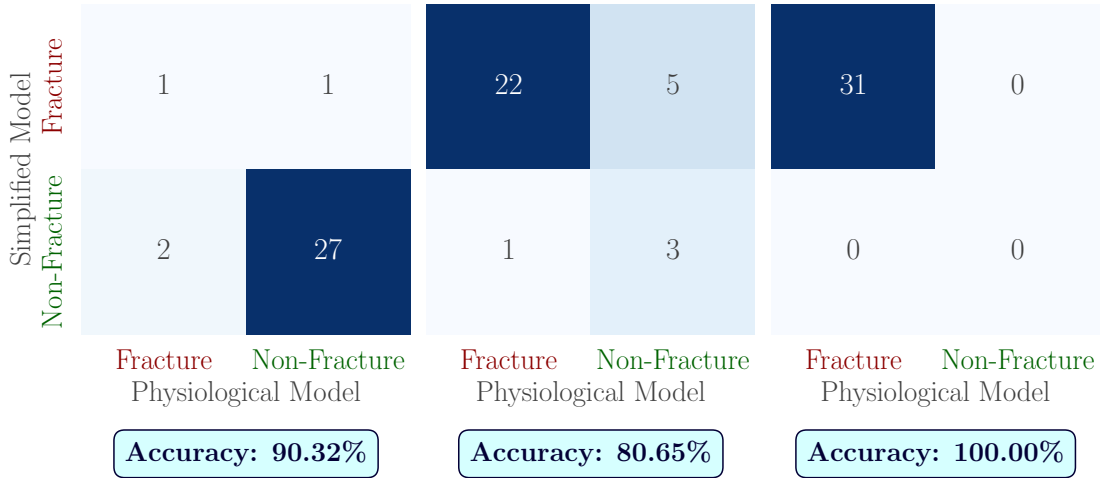

Figure 38: Confusion matrices of the fracture predictions divided in subgroups: safe (left), borderline (middle) and critical (right).

Spatial Investigation - Locations of Metastases

Locations of metastases causing prediction disagreement
The results presented in section 4.2.2 showed that certain bones with associated metastases led to differing fracture predictions between the simplified and the physiological model. The spatial distribution of these metastases within the femur is examined in the following and visualized in Fig. 39.

As it can be seen, nearly all metastases associated with prediction disagreement were located either in the inter-trochanteric region or the proximal femoral shaft. An exception was femur 880, where the metastasis was located at the transition between the femoral neck and the inter-trochanteric region.

No apparent dependency was observed between the type of prediction disagreement (physiological: fracture / simplified: non-fracture vs. physiological: non-fracture / simplified: fracture) and the anatomical location of the metastasis.

Furthermore, no systematic pattern could be identified that the positioning in the sagittal plane had an influence on the prediction agreement. All lesions affected the femoral cortex.

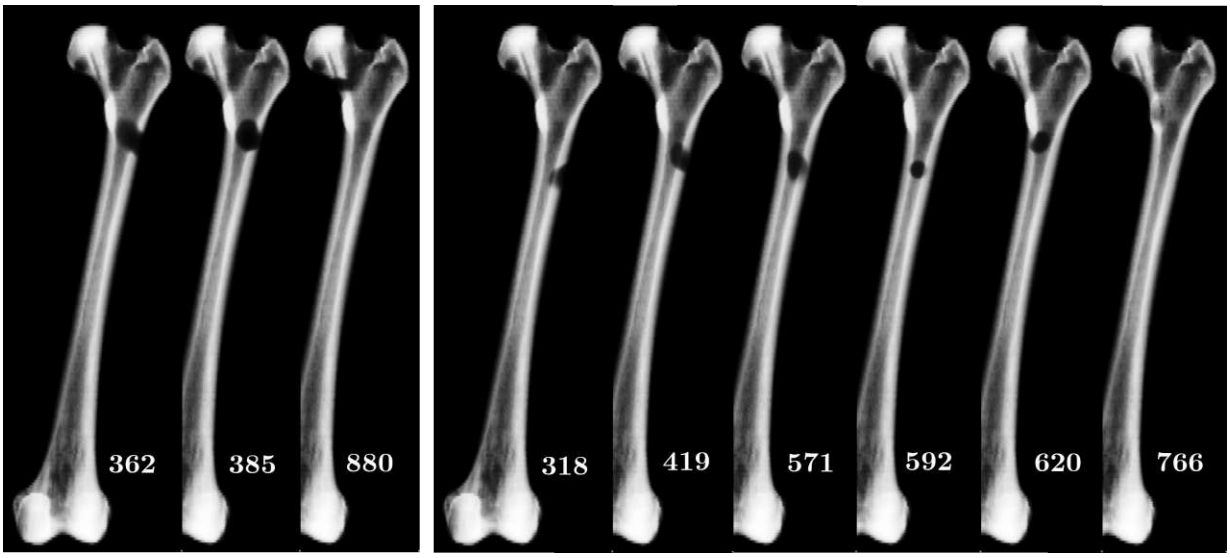

Figure 39: Projections of bones with metastases that caused disagreements between the models:
Physiological: Fracture, Simplified: No-Fracture (left) -
Physiological: No-Fracture, Simplified: Fracture (right).

Agreement of fracture prediction dependent on metastases location
Apart from the investigation of metastases that led to divergent fracture predictions, the prediction agreement was evaluated with respect to the anatomical location of the lesions.

Therefore, the centres of all metastases were marked in an anterior-posterior projection of the femoral bone, illustrated in Fig. 40.

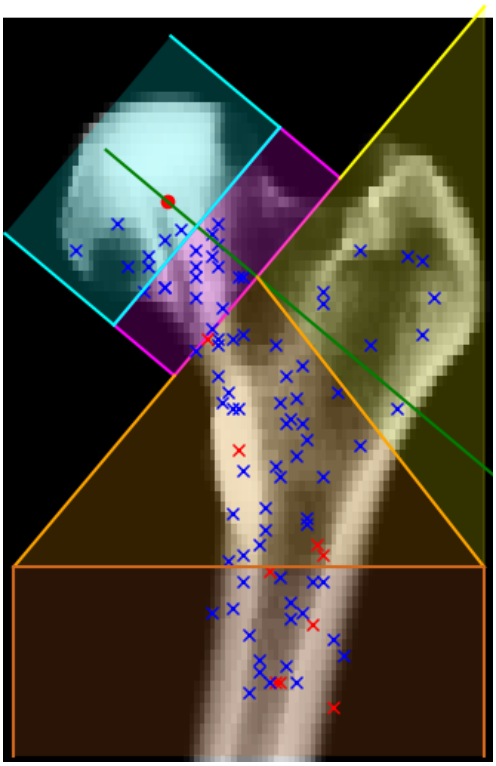

Figure 40: Femoral projection with the marked metastases centroids, colour-coded by prediction outcome: agreement (blue) and disagreement (red).

As illustrated in Fig. 40 and 41, model agreement reached 100% in the femoral head, greater trochanter and femoral neck RoI. In contrast, agreement in the intertrochanteric region was 89.74% and 78.26% in the proximal femoral shaft.

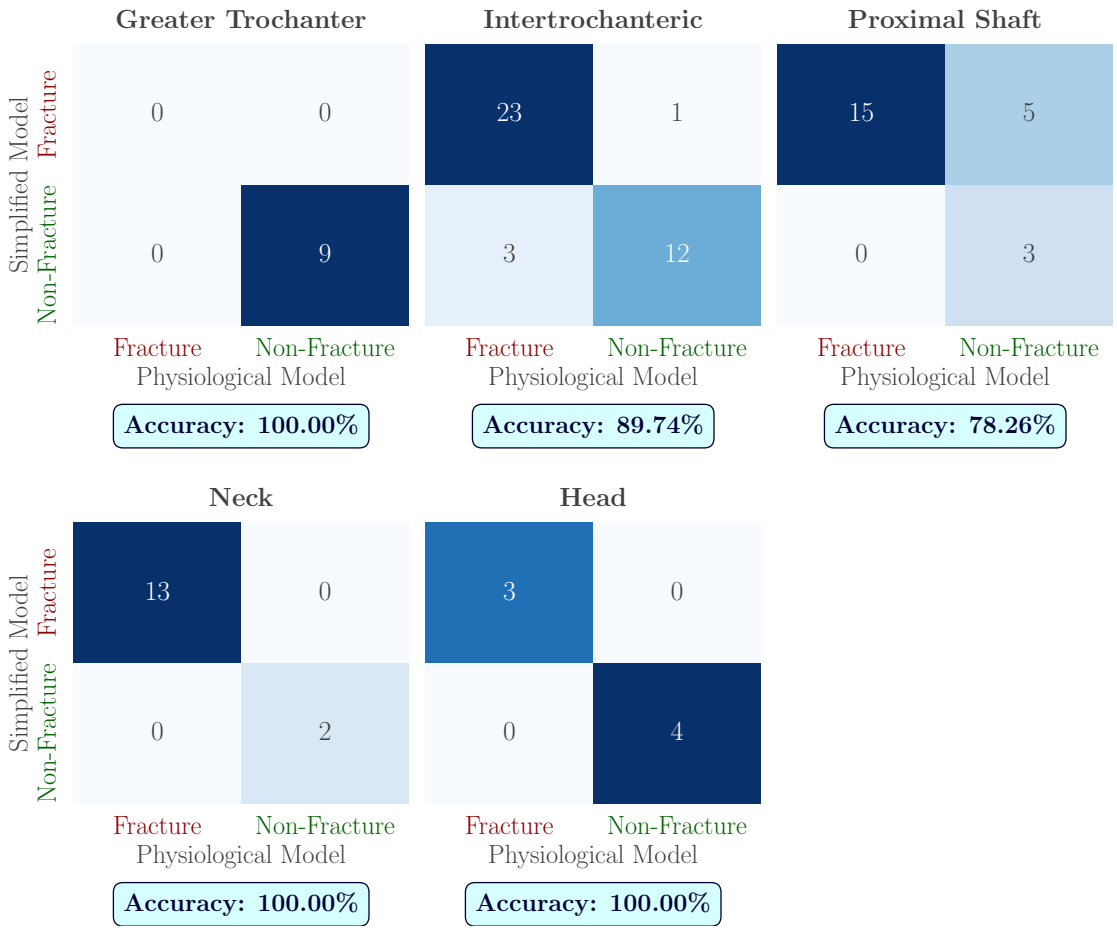

Figure 41: Confusion matrices of the fracture predictions divided by anatomical regions.

5 Discussion

The objectives of this study were (1) to develop a physiological FE model for activity-specific fracture risk assessment of a femur with an arbitrary metastatic lesion for the activity walking and (2) to compare the results with those of a simplified FE model on a large number of different artificial lytic lesions.

Based on simulations of 93 different artificial lesions in one femur, a high agreement (90.32 %) in fracture prediction was observed between the physiological and simplified FE models. Prediction disagreement was predominantly associated with metastatic lesions located in the proximal femoral shaft or the intertrochanteric region.

5.1 Model Comparison in the Intact Femur

5.1.1 Muscle and Hip Joint Forces

The muscle forces obtained through the musculoskeletal model and applied to physiological FE model were compared with results reported in literature in order to assess their plausibility. In this context, the studies by *Trinler et al.* [102] and Lin et al. [60] served as relevant references.

Trinler et al. comprises computed hip joint force and muscle force data for a selection of muscles based on ten healthy subjects (five female, five male; 28 ± 5 years) walking at a self-selected speed over ground, using the same underlying musculoskeletal model (Gait2392). Muscle and joint force results are given as mean values across all subjects, plus/minus one standard deviation, as shown in Figures 4 and 6 of the respective study [102]. Corresponding graphs of muscle and hip joint forces from the present study can be found in the appendix.
Overall, the computed muscle forces in the present study were in a comparable range to those reported by *Trinler et al.*. In most cases, they were within or near the upper bound of the reported standard deviation. Exceptions were the *Gastrocnemicus Medialis*, as well as the *Vastus Lateralis* and *Vastus Medialis*, which showed clearly higher peak forces in the present study.

The computed hip joint force in the present study closely matched the results reported by *Trinler et al.*, lying slightly below the reported mean value.

The differences in muscle force could be attributed to deviations in the modelling setup. Specifically, *Trinler et al.* implemented a SO cost function that minimized the sum of cubed muscle activations, i.e. $\sum a_i^3$, where a_i represents the activation of each muscle. This penalised higher individual muscle activations disproportionally, thus distributing the total muscle load across more muscles [24]. In contrast, the present study employed a cost function based on the sum of muscle activations squared, which still penalised higher individual muscle activations, but to a lesser extent, resulting in comparatively higher peak forces in individual muscles [24]. Since the identical net joint moments must be generated regardless of muscle activation patterns, it is plausible that the resulting joint force differs less, than the internal distribution of muscle forces.
Deviations in walking speed also affect both muscle and hip joint forces [3]; however, those deviations should be evenly reflected in muscle and hip joint forces. In order to be as accurate as possible, the model in the present study accounted for muscle force-length-velocity dependencies, contrarily to *Trinler et al.*. However, according to *Anderson and Pandy et al.* [6] such dependencies have little influence on the muscle force results for normal gait.

Additionally, the muscle and hip joint forces of this study were compared to the study by *Lin et al.* [60], who reported muscle force estimates based on one healthy individual (female, 25 years) walking at a velocity of 1.61 $\frac{\mathrm{m}}{\mathrm{s}}$ over ground, using the Gait2392 model. Muscle force results are shown in Figure 6 of the respective study [60]. Corresponding graphs of muscle forces from the present study are also provided in the appendix. In this case, the same cost function (squared muscle activations) was implemented and muscle force–length–velocity dependencies were taken into account.
Despite the modelling similarities, deviations in certain muscle forces were observed. In *Lin et al.*, the peak forces of the *Vastus* and the *Gastrocnemius* muscles were notably lower than those computed in the present study. In contrast, the *Gluteus Medius* and the combined *Ilio-Psoas* muscle, (*Iliacus* and *Psoas Major*) showed higher peaks in *Lin et al.* compared to the present study. The differences in muscle force may be attributed to variability in gait between subjects and to the higher walking speed in *Lin et al.* compared to the experimental subject in this study (1.36 $\frac{\mathrm{m}}{\mathrm{s}}$). However, an increase in walking speed typically results in generally higher forces across most muscles [3, 38]. In general, the findings demonstrate the fluctuation in musculoskeletal modelling outcomes, even when using the same musculoskeletal model and optimization criterion in the SO, due to presence of many influencing factors.

Overall, despite deviations in individual muscle force magnitudes, the computed muscle and hip joint forces fall within a plausible range compared to previously published data. This supports their suitability for the application in the physiological FE model in this study.

5.2 Model Comparison in Femora with Metastatic Lesions

5.2.1 Deformation and Stresses

In cases where both models predicted fracture, the majority of femora with artificial metastases showed similar patterns of plastic strain, especially when the metastatic lesion was large or located in the femoral neck. However, for smaller metastases or different locations, a notable number of cases still resulted in matching fracture prediction, yet showed differing plastic strain patterns. Interestingly, similar observations were made in studies comparing ultimate force and fracture location in ex vivo experiments with FE model predictions [27]. In these studies, often a good correlation of ultimate forces is observed despite a mismatch of the exact fracture location.

5.2.2 Agreement of Fracture Predictions

An overall accuracy of 90.32% in fracture prediction between the two models across the entire sample demonstrates a high level of agreement. Interestingly, the simplified model proved to be slightly more conservative than the physiological model. That suggests that muscle forces do not only act to increase load on the bone, but can also exert a stabilising, counteractive effect. In addition, the boundary conditions of the physiological model may inhibit excessive bending of the proximal femur.

Comparing the agreements in the "critical", "borderline" and "safe" subgroups, perfect and very good agreement was observed for the critical subgroup (accuracy: 100%) and subgroup safe (accuracy: 90.32%), respectively. As expected, almost all cases in the safe subgroup group were classified as non-fractured, with the physiological model being slightly more conservative. Regarding the borderline group, models still showed an acceptable agreement in fracture prediction with an accuracy of 80.65%. The tendency of the simplified model being the more conservative one was evident in this group (five out of six disagreement cases).

Spatial Investigation - Locations of Metastases

The spatial analysis showed that prediction disagreements between the simplified and physiological model were predominantly associated with lesions located in the proximal femoral shaft or the inter-trochanteric region near the lesser trochanter. Caution is therefore advised when relying on a simplified model for fracture prediction in this case. Until more precise differentiation is possible, the use of a safety factor is recommended for metastatic lesions located in the mentioned anatomical areas.
However, no clear trend was observed indicating that physiological models are more conservative. Using a larger sample comprising femora from multiple patients and more diverse metastatic lesions, may help to refine modelling suggestions depending on metastatic lesion location.

5.3 Limitations

There are several limitations in this study that should be acknowledged. First and foremost, the FE models were based on the femur of a single patient, which does not reflect the actual variability in bone morphology and structure across the population. Secondly, only one activity, namely walking, was investigated in this study. While the proposed workflow is in principle transferable to other physical activities, the agreement between physiological and simplified models may differ for other activities. Thirdly, the inserted metastatic lesions were artificially generated, since no CT scans with real metastatic lesions were available for this work and only lytic lesions in the proximal femur were investigated. Fourthly, the musculoskeletal model and the underlying kinematic data were scaled but not fully specific to this patient.

5.4 Conclusion

The results demonstrate that the simplified FE model, using only the proximal third of the femur and considering only for the peak hip joint force, achieves a high level of agreement (90.32 % accuracy) with the physiological model, that incorporates all muscle and hip joint forces throughout the full gait cycle. These findings support the validity of simplified FE models for fracture risk prediction in metastatic femora for the activity walking. As a conclusion, simplified models represent a promising balance between predictive accuracy and clinical feasibility for pathological fracture assessment during gait.

Nevertheless, the remaining disagreements between the two models, particularly in the region of the proximal femoral shaft and the lesser trochanter (78.26 % accuracy), as well as several limitations of this study warrant further investigation in this field. Future studies should be extended to more patients and different activities. Ultimately, simplified FE models have the potential to become a clinically viable tool for activity-specific fracture risk assessment, supporting clinical decision making and enhancing patients' quality of life.

6 Appendix

Comparison of muscle and hip joint forces with *Trinler et al.*:

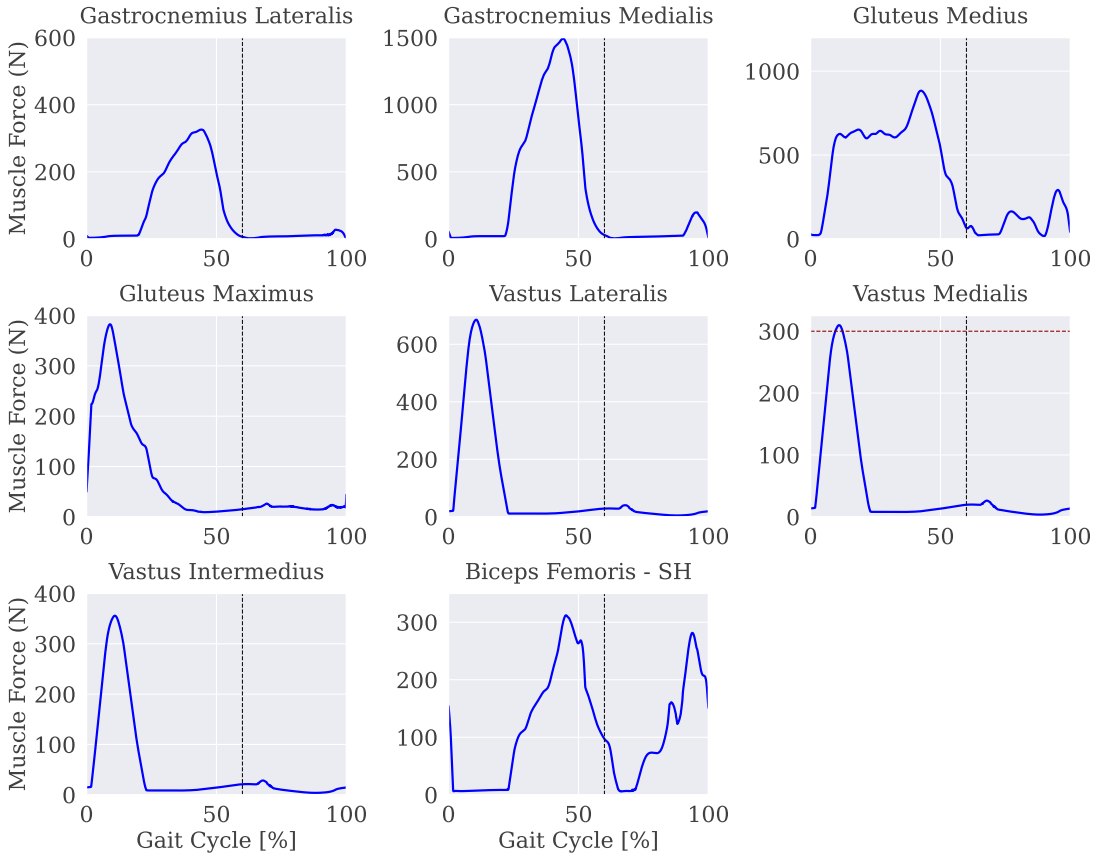

Figure 42: Resulting muscle forces of selected muscles for the comparison with *Trinler et al.*.

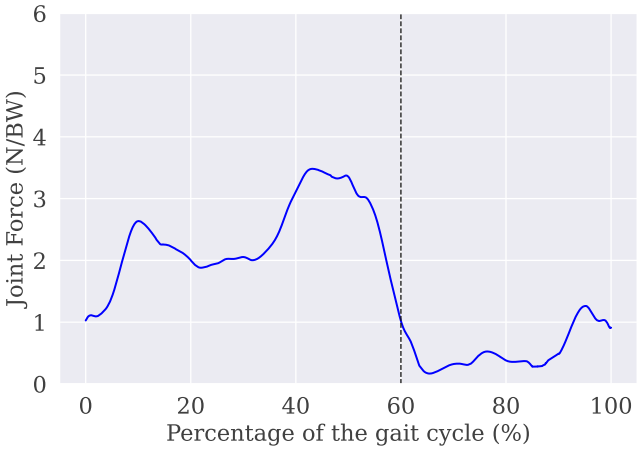

Figure 43: Resulting hip joint force for the comparison with *Trinler et al.*.

Comparison of muscle forces with *Lin et al.*:

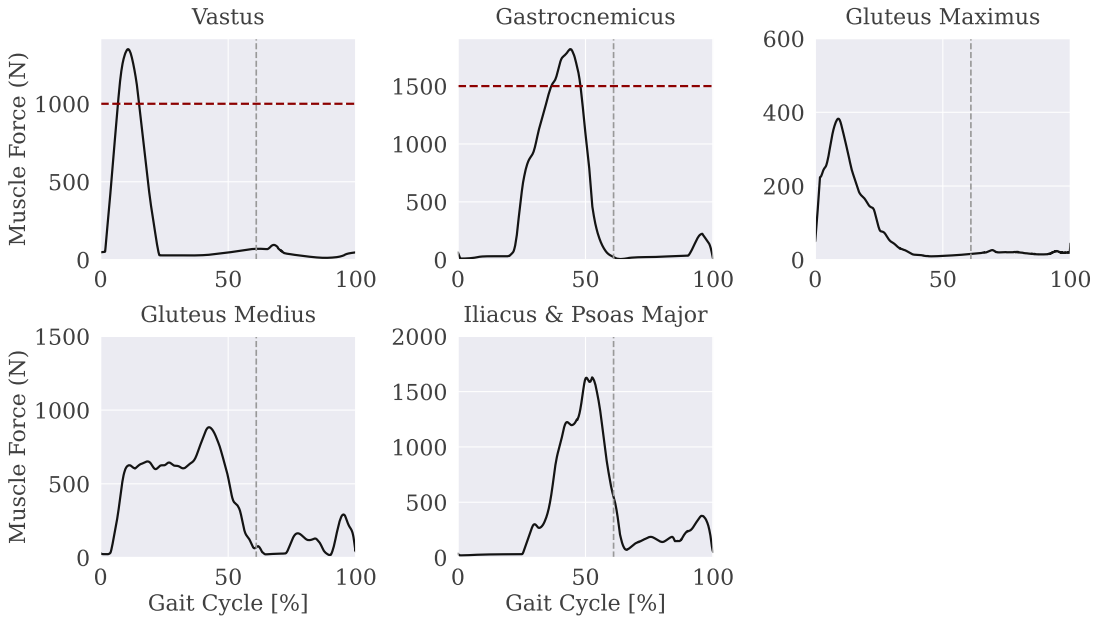

Figure 44: Resulting muscle forces of selected muscles for the comparison with *Lin et al.*.

Bibliography

[1] Angel Alberich-Bayarri et al. "Volume Mesh Generation and Finite Element Analysis of Trabecular Bone Magnetic Resonance Images". In: *Conference proceedings : ... Annual International Conference of the IEEE Engineering in Medicine and Biology Society. IEEE Engineering in Medicine and Biology Society. Conference* 2007 (Feb. 2007), pp. 1603–6. DOI: 10.1109/IEMBS.2007.4352612.

[2] Alessandra Aldieri et al. "HFValid collection: Hip-Fracture validation collection". Unpublished. 2023. URL: https://amsacta.unibo.it/id/eprint/7277/.

[3] Nathalie Alexander et al. "Effect of different walking speeds on joint and muscle force estimation using AnyBody and OpenSim". In: *Gait Posture* 90 (2021), pp. 197–203. ISSN: 0966-6362. DOI: https://doi.org/10.1016/j.gaitpost.2021.08.026. URL: https://www.sciencedirect.com/science/article/pii/S096663622100309X.

[4] Michael Skipper Andersen. "4 - Introduction to musculoskeletal modelling". In: *Computational Modelling of Biomechanics and Biotribology in the Musculoskeletal System (Second Edition)*. Ed. by Zhongmin Jin, Junyan Li, and Zhenxian Chen. Second Edition. Woodhead Publishing Series in Biomaterials. Woodhead Publishing, 2021, pp. 41–80. ISBN: 978-0-12-819531-4. DOI: https://doi.org/10.1016/B978-0-12-819531-4.00004-3. URL: https://www.sciencedirect.com/science/article/pii/B9780128195314000043.

[5] Frank Anderson and Marcus Pandy. "A Dynamic Optimization Solution for Vertical Jumping in Three Dimensions". In: *Computer methods in biomechanics and biomedical engineering* 2 (Feb. 1999), pp. 201–231. DOI: 10.1080/10255849908907988.

[6] Frank C. Anderson and Marcus G. Pandy. "Static and dynamic optimization solutions for gait are practically equivalent". In: *Journal of Biomechanics* 34.2 (2001), pp. 153–161. ISSN: 0021-9290. DOI: https://doi.org/10.1016/S0021-9290(00)00155-X. URL: https://www.sciencedirect.com/science/article/pii/S002192900000155X.

[7] Lorenzo Anez-Bustillos et al. "Finite element analysis and CT-based structural rigidity analysis to assess failure load in bones with simulated lytic defects". In: *Bone* 58 (2014), pp. 160–167. ISSN: 8756-3282. DOI: https://doi.org/10.1016/j.bone.2013.10.009. URL: https://www.sciencedirect.com/science/article/pii/S8756328213003876.

[8] Richard van Arkel et al. "Hip Abduction Can Prevent Posterior Edge Loading of Hip Replacements". In: *Journal of orthopaedic research : official publication of the Orthopaedic Research Society* 31 (Aug. 2013). DOI: 10.1002/jor.22364.

[9] Daniel Axelrod, Aaron Gazendam, and Michelle Ghert. "The Surgical Management of Proximal Femoral Metastases: A Narrative Review". In: *Current Oncology* 28 (Sept. 2021), pp. 3748–3757. DOI: 10.3390/curroncol28050320.

[10] Emir Benca et al. "QCT-based finite element prediction of pathologic fractures in proximal femora with metastatic lesions". In: *Scientific Reports* 9.1 (2019), p. 10305. DOI: 10.1038/s41598-019-46739-y.

[11] Emir Benca et al. "The insufficiencies of risk analysis of impending pathological fractures in patients with femoral metastases: A literature review". In: *Bone Reports* 5 (2016), pp. 51–56. ISSN: 2352-1872. DOI: https://doi.org/10.1016/j.bonr.2016.02.003. URL: https://www.sciencedirect.com/science/article/pii/S2352187216300080.

[12] Masahiko Bessho et al. "Prediction of strength and strain of the proximal femur by a CT-based finite element method". In: *Journal of Biomechanics* 40.8 (2007), pp. 1745–1753. ISSN: 0021-9290. DOI: https://doi.org/10.1016/j.jbiomech.2006.08.003. URL: https://www.sciencedirect.com/science/article/pii/S0021929006002879.

[13] Lucie Biehler-Gomez, Gaia Giordano, and Cristina Cattaneo. "The appearance of breast cancer metastases on dry bone: Implications for forensic anthropology". In: *Journal of Forensic and Legal Medicine* 61 (2019), pp. 5–12. ISSN: 1752-928X. DOI: https://doi.org/10.1016/j.jflm.2018.10.007. URL: https://www.sciencedirect.com/science/article/pii/S1752928X18303937.

[14] Thomas Buchanan et al. "Estimation of Muscle Forces and Joint Moments Using a Forward-Inverse Dynamics Model". In: *Medicine and science in sports and exercise* 37 (Dec. 2005), pp. 1911–6. DOI: 10.1249/01.mss.0000176684.24008.6f.

[15] M. R. Carhart. "Biomechanical Analysis of Compensatory Stepping: Implications for Paraplegics Standing Via FNS". PhD thesis. Arizona State University, 2000.

[16] Dennis Carter and Wilson Hayes. "Bone Compressive Strength: The Influence of Density and Strain Rate". In: *Science (New York, N.Y.)* 194 (Jan. 1977), pp. 1174–6. DOI: 10.1126/science.996549.

[17] Dmitry Chetverikov, Dmitry Stepanov, and Pavel Krsek. "Robust Euclidean alignment of 3D point sets: the trimmed iterative closest point algorithm". In: *Image and Vision Computing* 23.3 (2005), pp. 299–309. ISSN: 0262-8856. DOI: https://doi.org/10.1016/j.imavis.2004.05.007. URL: https://www.sciencedirect.com/science/article/pii/S0262885604001179.

[18] Dianna D. Cody et al. "Femoral strength is better predicted by finite element models than QCT and DXA". In: *Journal of Biomechanics* 32.10 (1999), pp. 1013–1020. ISSN: 0021-9290. DOI: https://doi.org/10.1016/S0021-9290(99)00099-8. URL: https://www.sciencedirect.com/science/article/pii/S0021929099000998.

[19] R. Coleman et al. "Bone health in cancer patients: ESMO Clinical Practice Guidelines†". In: *Annals of Oncology* 25 (2014). ESMO Updated Clinical Practice Guidelines, pp. iii124–iii137. ISSN: 0923-7534. DOI: https://doi.org/10.1093/annonc/mdu103. URL: https://www.sciencedirect.com/science/article/pii/S0923753419340785.

[20] Robert Coleman. "Metastatic bone disease: Clinical features, pathophysiology and treatment strategies". In: *Cancer treatment reviews* 27 (July 2001), pp. 165–76. DOI: 10.1053/ctrv.2000.0210.

[21] Robert E. Coleman et al. "Bone metastases". English (US). In: *Nature Reviews Disease Primers* 6.1 (Dec. 2020). Publisher Copyright: © 2020, Springer Nature Limited. ISSN: 2056-676X. DOI: 10.1038/s41572-020-00216-3.

[22] François H. Cornelis et al. "A Novel Implant for the Prophylactic Treatment of Impending Pathological Fractures of the Proximal Femur: Results from a Prospective, First-in-Man Study". In: *CardioVascular and Interventional Radiology* 40.7 (2017), pp. 1070–1076. ISSN: 1432-086X. DOI: 10.1007/s00270-017-1613-5. URL: https://doi.org/10.1007/s00270-017-1613-5.

[23] Luca Cristofolini et al. "In vitro replication of spontaneous fractures of the proximal human femur". In: *Journal of Biomechanics* 40.13 (2007), pp. 2837–2845. ISSN: 0021-9290. DOI: https://doi.org/10.1016/j.jbiomech.2007.03.015. URL: https://www.sciencedirect.com/science/article/pii/S0021929007001236.

[24] Roy D. Crowninshield and Richard A. Brand. "A physiologically based criterion of muscle force prediction in locomotion". In: *Journal of Biomechanics* 14.11 (1981), pp. 793–801. ISSN: 0021-9290. DOI: https://doi.org/10.1016/0021-9290(81)90035-X. URL: https://www.sciencedirect.com/science/article/pii/002192908190035X.

[25] Cristina Curreli et al. "Using musculoskeletal models to estimate in vivo total knee replacement kinematics and loads: Effect of differences between models". In: *Front. Bioeng. Biotechnol.* 9 (2021), p. 703508.

[26] John D. Currey. *Bones: Structure and Mechanics*. Princeton, NJ: Princeton University Press, 2002. ISBN: 978-0-691-09569-2.

[27] E. Dall'Ara et al. "A nonlinear QCT-based finite element model validation study for the human femur tested in two configurations in vitro". In: *Bone* 52.1 (2013), pp. 27–38. ISSN: 8756-3282. DOI: https://doi.org/10.1016/j.bone.2012.09.006. URL: https://www.sciencedirect.com/science/article/pii/S8756328212012306.

[28] Timothy Damron et al. "CT-based Structural Rigidity Analysis Is More Accurate Than Mirels Scoring for Fracture Prediction in Metastatic Femoral Lesions". In: *Clinical orthopaedics and related research* 474 (July 2015). DOI: 10.1007/s11999-015-4453-0.

[29] Scott Delp et al. "An interactive graphics-based model of the lower extremity to study orthopaedic surgical procedures". In: *IEEE transactions on bio-medical engineering* 37 (Sept. 1990), pp. 757–67. DOI: 10.1109/10.102791.

[30] Scott L. Delp et al. "OpenSim: Open-Source Software to Create and Analyze Dynamic Simulations of Movement". In: *IEEE Transactions on Biomedical Engineering* 54.11 (2007), pp. 1940–1950. DOI: 10.1109/TBME.2007.901024.

[31] Timothy D. DenOtter and Jason Schubert. "Hounsfield Unit". In: *StatPearls*. Updated March 6, 2023. Available from: https://www.ncbi.nlm.nih.gov/books/NBK547721/. Treasure Island (FL): StatPearls Publishing, 2023. URL: https://www.ncbi.nlm.nih.gov/books/NBK547721/.

[32] L. C. Derikx et al. "The assessment of the risk of fracture in femora with metastatic lesions: Comparing case-specific finite element analyses with predictions by clinical experts". In: *Journal of Bone and Joint Surgery. British Volume* 94-B.8 (2012), pp. 1135–1142. DOI: 10.1302/0301-620X.94B8.28449. URL: https://pubmed.ncbi.nlm.nih.gov/22844058/.

[33] Florieke Eggermont et al. "A Patient-Specific Fracture Risk Assessment Tool for Femoral Bone Metastases: Using the Bone Strength (BOS) Score in Clinical Practice". In: *Cancers* 14.23 (2022). ISSN: 2072-6694. DOI: 10.3390/cancers14235904. URL: https://www.mdpi.com/2072-6694/14/23/5904.

[34] Klaus Engelke, Bert Rietbergen, and Philippe Zysset. "FEA to Measure Bone Strength: A Review". In: *Clinical Reviews in Bone and Mineral Metabolism* 14 (Mar. 2016). DOI: 10.1007/s12018-015-9201-1.

[35] C. Ross Ethier and Craig A. Simmons. *Introductory Biomechanics: From Cells to Organisms*. Cambridge: Cambridge University Press, 2007. ISBN: 978-0-521-84609-7. URL: https://doi.org/10.1017/CBO9780511806407.

[36] Andriy Fedorov et al. "3D Slicer as an image computing platform for the Quantitative Imaging Network". In: *Magnetic Resonance Imaging* 30.9 (2012). Quantitative Imaging in Cancer, pp. 1323–1341. ISSN: 0730-725X. DOI: https://doi.org/10.1016/j.mri.2012.05.001. URL: https://www.sciencedirect.com/science/article/pii/S0730725X12001816.

[37] Henrique Ferrolho et al. "Inverse Dynamics vs. Forward Dynamics in Direct Transcription Formulations for Trajectory Optimization". In: May 2021, pp. 12752–12758. DOI: 10.1109/ICRA48506.2021.9561306.

[38] Carlos Fliger et al. "Effects of walking speed and age on the muscle forces of unimpaired gait subjects". In: *Journal of Physics: Conference Series* 705 (Apr. 2016), p. 012015. DOI: 10.1088/1742-6596/705/1/012015.

[39] Alessandro Franchi. "Epidemiology and classification of bone tumors". In: *Clinical cases in mineral and bone metabolism : the official journal of the Italian Society of Osteoporosis, Mineral Metabolism, and Skeletal Diseases* 9 (May 2012), pp. 92–5.

[40] James A. Friederich and Richard A. Brand. "Muscle fiber architecture in the human lower limb". In: *Journal of Biomechanics* 23.1 (1990), pp. 91–95. ISSN: 0021-9290. DOI: https://doi.org/10.1016/0021-9290(90)90373-B.

[41] N. Gelfand et al. "Robust Global Registration". In: *Proceedings of the 3rd Eurographics Symposium on Geometry Processing*. Jan. 2005.

[42] Christophe Geuzaine and Jean-François Remacle. "Gmsh: A 3-D finite element mesh generator with built-in pre- and post-processing facilities". In: *International Journal for Numerical Methods in Engineering* 79.11 (2009), pp. 1309–1331. DOI: 10.1002/nme.2579. URL: https://onlinelibrary.wiley.com/doi/abs/10.1002/nme.2579.

[43] Angela GGChang, Gregory Breeland, Austin C. Black, et al. "Anatomy, Bony Pelvis and Lower Limb: Femur". In: *StatPearls*. Treasure Island (FL): StatPearls Publishing, 2023. URL: https://www.ncbi.nlm.nih.gov/books/NBK532982/.

[44] Jacklyn R. Goodheart et al. "Simulating activities of daily living with finite element analysis improves fracture prediction for patients with metastatic femoral lesions". In: *Journal of Orthopaedic Research* 33.8 (2015), pp. 1226–1234. DOI: 10.1002/jor.22887. URL: https://onlinelibrary.wiley.com/doi/full/10.1002/jor.22887.

[45] Henry Gray and Henry Vandyke Carter. "Gray's Anatomy, 39th Edition: The Anatomical Basis of Clinical Practice". In: *American Journal of Neuroradiology* 26.10 (2005). Ed. by American Society of Neuroradiology, pp. 2703–2704. ISSN: 0195-6108. eprint: http://www.ajnr.org/content/26/10/2703.pdf. URL: http://www.ajnr.org/content/26/10/2703.

[46] Emer M. Guinan et al. "Associations Among Physical Activity, Skeletal Related Events, and Patient Reported Outcomes in Patients with Bone Metastases". In: *Seminars in Oncology Nursing* 38.2 (2022). Bone Health, p. 151274. ISSN: 0749-2081. DOI: https://doi.org/10.1016/j.soncn.2022.151274. URL: https://www.sciencedirect.com/science/article/pii/S0749208122000274.

[47] William D. Hage, Albert J. Aboulafia, and David M. Aboulafia. "INCIDENCE, LOCATION, AND DIAGNOSTIC EVALUATION OF METASTATIC BONE DISEASE". In: *Orthopedic Clinics of North America* 31.4 (2000), pp. 515–528. ISSN: 0030-5898. DOI: https://doi.org/10.1016/S0030-5898(05)70171-1. URL: https://www.sciencedirect.com/science/article/pii/S0030589805701711.

[48] B. Helgason et al. "The influence of the modulus–density relationship and the material mapping method on the simulated mechanical response of the proximal femur in side-ways fall loading configuration". In: *Medical Engineering Physics* 38.7 (2016), pp. 679–689. ISSN: 1350-4533. DOI: https://doi.org/10.1016/j.medengphy.2016.03.006. URL: https://www.sciencedirect.com/science/article/pii/S135045331630039X.

[49] M. G. Hoy, F. E. Zajac, and M. E. Gordon. "A musculoskeletal model of the human lower extremity: the effect of muscle, tendon, and moment arm on the moment-angle relationship of musculotendon actuators at the hip, knee, and ankle". In: *J. Biomech.* 23 (1990), pp. 157–169.

[50] V.T. Inman. *The Joints of the Ankle*. Williams and Wilkins, 1976.

[51] Takuya Ishimoto et al. "Trabecular health of vertebrae based on anisotropy in trabecular architecture and collagen/apatite micro-arrangement after implantation of intervertebral fusion cages in the sheep spine". In: *Bone* 108 (2018), pp. 25–33. ISSN: 8756-3282. DOI: https://doi.org/10.1016/j.bone.2017.12.012. URL: https://www.sciencedirect.com/science/article/pii/S8756328217304507.

[52] Christopher R. Jacobs et al. "Numerical instabilities in bone remodeling simulations: The advantages of a node-based finite element approach". In: *Journal of Biomechanics* 28.4 (1995), pp. 449–459. ISSN: 0021-9290. DOI: https://doi.org/10.1016/0021-9290(94)00087-K. URL: https://www.sciencedirect.com/science/article/pii/002192909400087K.

[53] Chand John et al. "Stabilisation of walking by intrinsic muscle properties revealed in a three-dimensional muscle-driven simulation". In: *Computer methods in biomechanics and biomedical engineering* 16 (Jan. 2012). DOI: 10.1080/10255842.2011.627560.

[54] Joshua Johnson et al. "Finite Element Model-Computed Mechanical Behavior of Femurs with Metastatic Disease Varies Between Physiologic and Idealized Loading Simulations". In: *Biomedical Engineering and Computational Biology* 14 (Mar. 2023), p. 117959722311662. DOI: 10.1177/11795972231166240.

[55] Hans Kainz et al. "Reliability of four models for clinical gait analysis". In: *Gait and Posture* 54 (2017), pp. 325–331. ISSN: 0966-6362. DOI: 10.1016/j.gaitpost.2017.04.001.

[56] Tadashi S. Kaneko et al. "Relationships between material properties and CT scan data of cortical bone with and without metastatic lesions". In: *Medical Engineering Physics* 25.6 (2003), pp. 445–454. ISSN: 1350-4533. DOI: https://doi.org/10.1016/S1350-4533(03)00030-4. URL: https://www.sciencedirect.com/science/article/pii/S1350453303000304.

[57] Joyce Keyak et al. "Predicting Proximal Femoral Strength Using Structural Engineering Models". In: *Clinical orthopaedics and related research* andNA; (Sept. 2005), pp. 219–28. DOI: 10.1097/01.blo.0000164400.37905.22.

[58] Joyce Keyak et al. "Predicting the Strength of Femoral Shafts with and without Metastatic Lesions". In: *Clinical orthopaedics and related research* 439 (Nov. 2005), pp. 161–70. DOI: 10.1097/01.blo.0000174736.50964.3b.

[59] Steven Lautzenheiser, Adam Sylvester, and Patricia Kramer. "A review of musculoskeletal modeling of human locomotion". In: *Interface Focus* (Aug. 2021).

[60] Yi-Chung Lin et al. "Comparison of different methods for estimating muscle forces in human movement". In: *Proceedings of the Institution of Mechanical Engineers, Part H* 226.2 (2012). PMID: 22468462, pp. 103–112. DOI: 10.1177/0954411911429401. URL: https://doi.org/10.1177/0954411911429401.

[61] Yvette Linden et al. "Comparative analysis of risk factors for pathological fracture with femoral metastases: Results based on a randomised trial of radiotherapy". In: *The Journal of bone and joint surgery. British volume* 86 (May 2004), pp. 566–73.

[62] B. Luisier, E. Dall'Ara, and D.H. Pahr. "Orthotropic HR-pQCT-based FE models improve strength predictions for stance but not for side-way fall loading compared to isotropic QCT-based FE models of human femurs". In: *Journal of the Mechanical Behavior of Biomedical Materials* 32 (2014), pp. 287–299. ISSN: 1751-6161. DOI: https://doi.org/10.1016/j.jmbbm.2014.01.006. URL: https://www.sciencedirect.com/science/article/pii/S1751616114000071.

[63] Filipa Macedo et al. "Bone Metastases: An Overview". In: *Oncology Reviews* 11.1 (2017), p. 321. DOI: 10.4081/oncol.2017.321. URL: https://www.ncbi.nlm.nih.gov/pmc/articles/PMC5444408/.

[64] Matthew Millard et al. "Flexing Computational Muscle: Modeling and Simulation of Musculotendon Dynamics". In: *Journal of Biomechanical Engineering* 135.2 (2013), p. 021005. DOI: 10.1115/1.4023390. URL: https://doi.org/10.1115/1.4023390.

[65] H Mirels. "Metastatic disease in long bones. A proposed scoring system for diagnosing impending pathologic fractures". In: *Clinical orthopaedics and related research* 249 (Dec. 1989), pp. 256–264. ISSN: 0009-921X.

[66] Niloy J. Mitra et al. "Registration of point cloud data from a geometric optimization perspective". In: *Proceedings of the 2004 Eurographics/ACM SIGGRAPH Symposium on Geometry Processing*. SGP '04. Nice, France: Association for Computing Machinery, 2004, pp. 22–31. ISBN: 3905673134.

DOI: 10.1145/1057432.1057435. URL: https://doi.org/10.1145/1057432.1057435.

[67] Luca Modenese. *MuscleForceDirection: an OpenSim plugin to extract the muscle lines of action and attachments*. User Guide. Dec. 2020. URL: https://simtk.org/home/force_direction.

[68] Elise F. Morgan, Ginu U. Unnikrisnan, and Amira I. Hussein. "Bone Mechanical Properties in Healthy and Diseased States". In: *Annual Review of Biomedical Engineering* 20 (2018), pp. 119–143. ISSN: 1523-9829. DOI: 10.1146/annurev-bioeng-062117-121139. URL: https://www.annualreviews.org/doi/10.1146/annurev-bioeng-062117-121139.

[69] Gregory Mundy. "Metastasis to bone: Causes, consequences and therapeutic opportunities". In: *Nature reviews. Cancer* 2 (Sept. 2002), pp. 584–93. DOI: 10.1038/nrc867.

[70] J.Z. Zhu O. C. Zienkiewicz R. L. Taylor. *The Finite Element Method: Its Basis and Fundamentals*. Elsevier, 2005. URL: https://api.semanticscholar.org/CorpusID:260666725.

[71] OpenSim Team. *OpenSim Documentation - Inverse Kinematics*. (accessed: 08.03.2025). 2025. URL: https://opensimconfluence.atlassian.net/wiki/spaces/OpenSim/pages/53090037/Inverse+Kinematics.

[72] OpenSim Team. *OpenSim Documentation - Residual Reduction Algorithm*. (accessed: 09.03.2025). 2025. URL: https://opensimconfluence.atlassian.net/wiki/spaces/OpenSim/pages/53089669/Residual+Reduction+Algorithm.

[73] OpenSim Team. *OpenSim Documentation - Static Optimization*. (accessed: 10.03.2025). 2025. URL: https://opensimconfluence.atlassian.net/wiki/spaces/OpenSim/pages/53090088/Static+Optimization.

[74] OpenSim-Team. *OpenSim Documentation - OpenSim Models*. (accessed: 01.05.2025). 2025. URL: https://opensimconfluence.atlassian.net/wiki/spaces/OpenSim/pages/53088473/OpenSim+Models.

[75] OpenSim-Team. *OpenSim Documentation - Scaling*. (accessed: 08.03.2025). 2025. URL: https://opensimconfluence.atlassian.net/wiki/spaces/OpenSim/pages/53090000/Scaling.

[76] OpenSim-Team. *OpenSim Documentation - Thelen 2003 Muscle Model*. (accessed: 01.05.2025). 2025. URL: https://opensimconfluence.atlassian.net/wiki/spaces/OpenSim/pages/53089814/Thelen+2003+Muscle+Model.

[77] Dieter Pahr, Alexander Synek, and Saeideh Saeidi. *Finite Element Methoden in der Biomechanik*. Lecture Slides, Institut für Leichtbau und Struktur-Biomechanik. 2022.

[78] Dieter H. Pahr et al. "HR-pQCT-based homogenised finite element models provide quantitative predictions of experimental vertebral body stiffness and strength with the same accuracy as μFE models". In: *Computer Methods in Biomechanics and Biomedical Engineering* 15.7 (2012), pp. 711–720. DOI: 10.1080/10255842.2011.556627. eprint: https://doi.org/10.1080/10255842.2011.556627. URL: https://doi.org/10.1080/10255842.2011.556627.

[79] J. Panyasantisuk et al. "Mapping anisotropy improves QCT-based finite element estimation of hip strength in pooled stance and side-fall load configurations". In: *Medical Engineering Physics* 59 (2018), pp. 36–42. ISSN: 1350-4533. DOI: https://doi.org/10.1016/j.medengphy.2018.06.004. URL: https://www.sciencedirect.com/science/article/pii/S1350453318300997.

[80] Liang Peng et al. "Comparison of isotropic and orthotropic material property assignments on femoral finite element models under two loading conditions". In: *Medical Engineering Physics* 28.3 (2006), pp. 227–233. ISSN: 1350-4533. DOI: https://doi.org/10.1016/j.medengphy.2005.06.003. URL: https://www.sciencedirect.com/science/article/pii/S1350453305001359.

[81] Andrew T.M. Phillips, Claire C. Villette, and Luca Modenese and. "Femoral bone mesoscale structural architecture prediction using musculoskeletal and finite element modelling". In: *International Biomechanics* 2.1 (2015), pp. 43–61. DOI: 10.1080/23335432.2015.1017609.

[82] Jae-Young Rho, Liisa Kuhn-Spearing, and Peter Zioupos. "Mechanical properties and the hierarchical structure of bone". In: *Medical Engineering Physics* 20.2 (1998), pp. 92–102. ISSN: 1350-4533. DOI: https://doi.org/10.1016/S1350-4533(98)00007-1. URL: https://www.sciencedirect.com/science/article/pii/S1350453398000071.

[83] Sarah Roelker et al. "Interpreting Musculoskeletal Models and Dynamic Simulations: Causes and Effects of Differences Between Models". In: *Annals of Biomedical Engineering* 45 (2017). DOI: 10.1007/s10439-017-1894-5.

[84] B. M. Rothschild, I. Hershkovitz, and O. Dutour. "Clues Potentially Distinguishing Lytic Lesions of Multiple Myeloma From Those of Metastatic Carcinoma". In: *American Journal of Physical Anthropology*

105.2 (1998), pp. 241–250. DOI: 10.1002/(SICI)1096-8644(199802)105:2<241::AID-AJPA10>3.0.CO;2-0. URL: https://pubmed.ncbi.nlm.nih.gov/9511917/.

[85] A. Ruggiero, R. D'Amato, and S. Affatato. "Comparison of meshing strategies in thr finite element modelling". In: *Materials* 12 (14 2019), p. 2332. DOI: 10.3390/ma12142332.

[86] Amelie Sas et al. "Finite element models for fracture prevention in patients with metastatic bone disease. A literature review". In: *Bone Reports* 12 (2020), p. 100286. ISSN: 2352-1872. DOI: https://doi.org/10.1016/j.bonr.2020.100286. URL: https://www.sciencedirect.com/science/article/pii/S2352187220300462.

[87] Amelie Sas et al. "Nonlinear voxel-based finite element model for strength assessment of healthy and metastatic proximal femurs". In: *Bone Reports* 12 (2020), p. 100263. ISSN: 2352-1872. DOI: https://doi.org/10.1016/j.bonr.2020.100263. URL: https://www.sciencedirect.com/science/article/pii/S2352187220300231.

[88] Giovanni Selvaggi and Giorgio V. Scagliotti. "Management of bone metastases in cancer: A review". In: *Critical Reviews in Oncology/Hematology* 56.3 (2005), pp. 365–378. ISSN: 1040-8428. DOI: https://doi.org/10.1016/j.critrevonc.2005.03.011. URL: https://www.sciencedirect.com/science/article/pii/S1040842805000661.

[89] Ajay Seth et al. "OpenSim: a musculoskeletal modeling and simulation framework for in silico investigations and exchange". In: *Procedia IUTAM* 2 (2011). IUTAM Symposium on Human Body Dynamics, pp. 212–232. ISSN: 2210-9838. DOI: https://doi.org/10.1016/j.piutam.2011.04.021. URL: https://www.sciencedirect.com/science/article/pii/S2210983811000228.

[90] Ajay Seth et al. "OpenSim: Simulating musculoskeletal dynamics and neuromuscular control to study human and animal movement". In: *PLOS Computational Biology* 14.7 (2018), e1006223. DOI: 10.1371/journal.pcbi.1006223. URL: https://doi.org/10.1371/journal.pcbi.1006223.

[91] Riemer Slart et al. "Updated practice guideline for dual-energy X-ray absorptiometry (DXA)". In: *European Journal of Nuclear Medicine and Molecular Imaging* 52 (Sept. 2024), pp. 539–563. DOI: 10.1007/s00259-024-06912-6.

[92] Andrew D. Speirs et al. "Physiologically based boundary conditions in finite element modelling". In: *Journal of Biomechanics* 40 (2007), pp. 2318–2323. ISSN: 0021-9290. DOI: https://doi.org/10.1016/j.jbiomech.2006.10.038. URL: https://www.sciencedirect.com/science/article/pii/S0021929006004076.

[93] Marc A. Stadelmann et al. "Conventional finite element models estimate the strength of metastatic human vertebrae despite alterations of the bone's tissue and structure". In: *Bone* 141 (2020), p. 115598. ISSN: 8756-3282. DOI: https://doi.org/10.1016/j.bone.2020.115598. URL: https://www.sciencedirect.com/science/article/pii/S8756328220303781.

[94] Amir Sternheim et al. "Pathological fracture risk assessment in patients with femoral metastases using CT-based finite element methods. A retrospective clinical study". In: *Bone* 110 (2018), pp. 215–220. ISSN: 8756-3282. DOI: https://doi.org/10.1016/j.bone.2018.02.011. URL: https://www.sciencedirect.com/science/article/pii/S875632821830070X.

[95] Jay Stock. "Wolff's law (bone functional adaptation)". In: (Oct. 2018), pp. 1–2. DOI: 10.1002/9781118584538.ieba0521.

[96] D. L. Stredney. "The representation of anatomical structures through computer animation for scientific, educational and artistic applications". MA thesis. The Ohio State University, 1982.

[97] Alexander Synek et al. "Predicting strength of femora with metastatic lesions from single 2D radiographic projections using convolutional neural networks". In: *Computer Methods and Programs in Biomedicine* 265 (2025), p. 108724. ISSN: 0169-2607. DOI: https://doi.org/10.1016/j.cmpb.2025.108724. URL: https://www.sciencedirect.com/science/article/pii/S0169260725001415.

[98] Esther Tanck et al. "Pathological fracture prediction in patients with metastatic lesions can be improved with quantitative computed tomography based computer models". In: *Bone* 45.4 (2009), pp. 777–783. ISSN: 8756-3282. DOI: https://doi.org/10.1016/j.bone.2009.06.009. URL: https://www.sciencedirect.com/science/article/pii/S8756328209016329.

[99] Zuzana Tatar et al. "Assessment of the risk factors for impending fractures following radiotherapy for long bone metastases using CT scan-based virtual simulation: a retrospective study". In: *Radiation oncology (London, England)* 9 (Oct. 2014), p. 227. DOI: 10.1186/s13014-014-0227-1.

[100] OpenSim Team. *OpenSim Documentation - Gait 2392 and 2354 Models*. (accessed: 08.03.2025). 2025. URL: https://opensimconfluence.atlassian.net/wiki/spaces/OpenSim/pages/53086215/Gait+2392+and+2354+Models.

[101] OpenSim Team. *OpenSim Documentation - Joint Reactions Analysis*. (accessed: 10.03.2025). 2025. URL: https://opensimconfluence.atlassian.net/wiki/spaces/OpenSim/pages/53089600/Joint+Reactions+Analysis.

[102] Ursula Trinler et al. "Muscle force estimation in clinical gait analysis using AnyBody and OpenSim". In: *Journal of Biomechanics* 86 (2019), pp. 55–63. ISSN: 0021-9290. DOI: https://doi.org/10.1016/j.jbiomech.2019.01.045. URL: https://www.sciencedirect.com/science/article/pii/S002192901930082X.

[103] T. L. Wickiewicz et al. "Muscle architecture of the human lower limb". In: *Clin. Orthop. Rel. Res.* 179 (1983), pp. 275–283.

[104] Wikimedia Commons contributors - Johanna Diedrich. *Anatomie des Knochens und physiologisches Knochenremodeling2*. Image licensed under CC BY-SA 4.0. Accessed on 2025-05-13. 2021. URL: https://commons.wikimedia.org/wiki/File:Anatomie_des_Knochens_und_physiologisches_Knochenremodeling2.png.

[105] Gary Tad Yamaguchi et al. "A planar model of the knee joint to characterize the knee extensor mechanism." In: *Journal of biomechanics* 22 1 (1989), pp. 1–10. URL: https://api.semanticscholar.org/CorpusID:25954756.

[106] Zohar Yosibash et al. "Predicting the stiffness and strength of human femurs with real metastatic tumors". In: *Bone* 69 (2014), pp. 180–190. ISSN: 8756-3282. DOI: https://doi.org/10.1016/j.bone.2014.09.022. URL: https://www.sciencedirect.com/science/article/pii/S8756328214003615.

[107] P.K. Zysset and A. Curnier. "An alternative model for anisotropic elasticity based on fabric tensors". In: *Mechanics of Materials* 21.4 (1995), pp. 243–250. ISSN: 0167-6636. DOI: https://doi.org/10.1016/0167-6636(95)00018-6. URL: https://www.sciencedirect.com/science/article/pii/0167663695000186.

[108] Philippe Zysset et al. "Finite element analysis for prediction of bone strength". In: *BoneKEy reports* 2 (Aug. 2013), p. 386. DOI: 10.1038/bonekey.2013.120.